

# **A Novel Soil Moisture Retrieval Algorithm for FY-3E GNOS-R Leveraging Multi-Angle Observations**

Xuerui WU<sup>1</sup>, Junming XIA<sup>2</sup>, Weihua BAI<sup>2</sup>, & Yueqiang SUN<sup>2</sup>

1. Shanghai Astronomical Observatory, Chinese Academy of Sciences, Shanghai 200030, China (e-mail:  
xrwu@shao.ac.cn).

2. National Space Science Centers, Chinese Academic of Sciences, Beijing 100190, China

**Xuerui WU:** 提出研究思路, 设计研究方案; 负责实验; 起草论文;

**Junming XIA:** 提出研究思路, 设计研究方案;

**Weihua BAI:** 负责采集、清洗和分析数据;

**Yueqiang SUN:** 负责最终版本修订。

---

\* Corresponding author: Xuerui WU (E-mail: xrwu@shao.ac.cn).

## **Abstract**

**Objective:** Develop effective FY-3E GNOS-R algorithm for global soil moisture retrieval.

**Methods:**

1. Incorporate first-order vegetation model, consider density, and volume scattering.
2. Use multi-angle GNOS-R observations, combine with SMAP data for optimization.
3. Tailor algorithm for diverse surface conditions; parameterize surface roughness based on angle.

**Results:** Achieve enhanced retrieval accuracy, RMSE: 0.0235, 0.0264, 0.0191 (g/cm<sup>3</sup>) for bare, low vegetation, and dense vegetation areas.

**Limitations:** Limited to one month of data; further testing required for broader applicability.

**Conclusions:** GNOS-R proves a robust tool, surpassing previous techniques for global soil moisture estimation.

**Keywords:** GNSS-Reflectometry; GNOS-R; soil moisture; SMAP

## 1. Introduction

Surface soil moisture (SM) is pivotal in controlling the exchange of water and energy between land surfaces and the atmosphere. This makes it crucial for hydrological modeling, agricultural management, and numerical weather forecasting.

Over the past three decades, Global Navigation Satellite System-Reflectometry (GNSS-R) has emerged as a promising remote sensing technique, garnering increasing interest from the scientific community [1-2]. While its initial applications predominantly focused on ocean surface studies, its scope has expanded to land surface analyses [3]. However, the development of land surface applications remains challenging due to the complexity of land surface geophysical parameters. These applications include soil moisture estimation, vegetation biomass measurement, flood inundation mapping, and soil freeze/thaw detection [4-7]. Among these applications, soil moisture monitoring via GNSS-R is currently a rapidly expanding field, given that the L-band has been identified as an optimal frequency for soil moisture monitoring.

Following the implementation of soil moisture monitoring using ground-based GPS receivers, several space-borne GNSS-R missions have been launched in the last two decades, each contributing to the advancement of this field. For instance, the UK DMC, the first mission commenced in 2003, demonstrated the potential of GNSS-R for soil moisture detection [8]. The TechDemoSat-1 (TDS-1) satellite, launched in 2014, has provided valuable insights into soil moisture monitoring, despite ceasing operations in 2019 [9]. NASA's Cyclone Global Navigation Satellite System (CYGNSS), launched in 2016, initially intended for oceanic hurricane studies, has also facilitated efficient soil moisture retrieval research [10]. Subsequent missions such as WINSAT-1R, UK-Dot-1, and China's first GNSS-R satellite mission, BuFeng-1 A/B, launched in 2017, 2019, and 2019, respectively, further expanded the GNSS-R payloads [11]. Future GNSS-R missions include ESA's HydroGNSS, scheduled for launch in 2024, targeting four hydrological ECVs, one of which is soil moisture [12]. The FengYun-3E (FY-3E), the fifth satellite in China's polar orbiting meteorological satellite series, embodies a new generation of GNSS-R sensor, the GNSS Occultation Sounder II (GNOS-II) [13]. The GNOS-II consists of the GNSS-Radio occultation payload and the GNSS-Reflectometry payload, the latter referred to as GNOS-R. One of the critical attributes of GNOS-R is its global coverage.

Figure 1 provides an overview of the evolution of space-borne GNSS-R missions or payloads. Notably, the upcoming ESA's HydroGNSS, together with existing missions like SMOS and SMAP, will provide continuity between existing and future L-band missions [14,15].

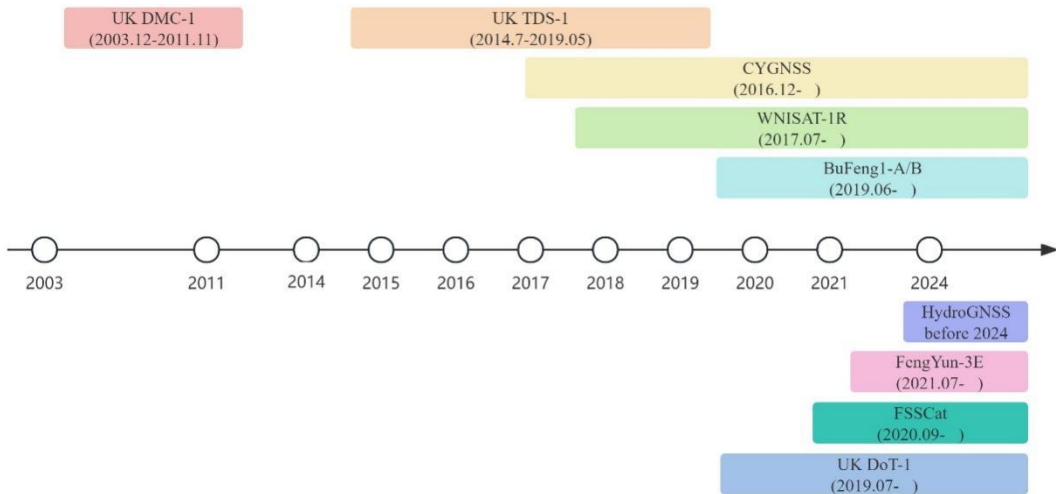


**Figure 1** The development of space-borne GNSS-R missions or payloads.

Distinct from traditional radar or radiometer technologies, GNSS-R operates as a bistatic or multi-static radar and offers unique features arising from its changing measurement geometry. In other words, with GNSS-R, the locations of specular points and incidence angles along the satellite track vary with the movement of GNSS transmitters and GNSS-R receivers. This variability results in changing footprint areas, making it impossible to precisely repeat the same measurement conditions from orbit to orbit. Most of the present works have not taken the detailed information of the incidence angle into consideration[16-21].

While Al Khaldi et al.[22] proposed a method to correct the impact of incidence angle on GNSS-R surface effective reflectivity, this is to normalize the reflectivity of different signal incidence angles to the sky nadir direction. As shown in Figure 3.6 (a), the correlation curve between the reflectivity of GPS L1 carrier signal and the signal incidence angle under different soil moisture conditions is given. Under the same soil moisture condition, the surface reflectivity under different incident angles is divided by the reflectivity of the incident signal in the nadir direction and this method is to standardize the incidence angles. However, this kind of treatment will lose the valuable information in the observation geometry. In this study, we propose an improved soil moisture retrieval method using GNSS-R data that leverages observation geometry information. Unique to this approach is the use of specular incidence angle data to correct the effects of surface roughness and vegetation – two critical factors influencing the final soil moisture accuracy. By utilizing the observation geometry information, we note that surface roughness varies for different specular incidence angles. This observation allows us to derive distinct roughness coefficients based on the observation geometry. Unlike previous studies that used normalization angle information, our method applies the zero-order and first order scattering model to correct vegetation effects according to the observation geometry.

This approach retains valuable information in the observation geometry, which would be lost through normalization methods.

The remainder of the paper is organized as follows: Section 2 presents the datasets and methodology. Section 3 results and analysis, while section 4 presents the discussion and Section 5 concludes with potential future work for GNOS-R.

## 2. Datasets

### 2.1 FY-3E GNOS-R Dataset

Delay-Doppler Mapping (DDM) is the original observation of GNSS R. Compared to the conventional uniform DDM from TDS-1 and CYGNSS Level 1 products, the DDM generated by the GNOS-R receiver is non-uniform, which will be able to obtain more sampling near the specular point. An onboard DDM is presented in Figure 2.

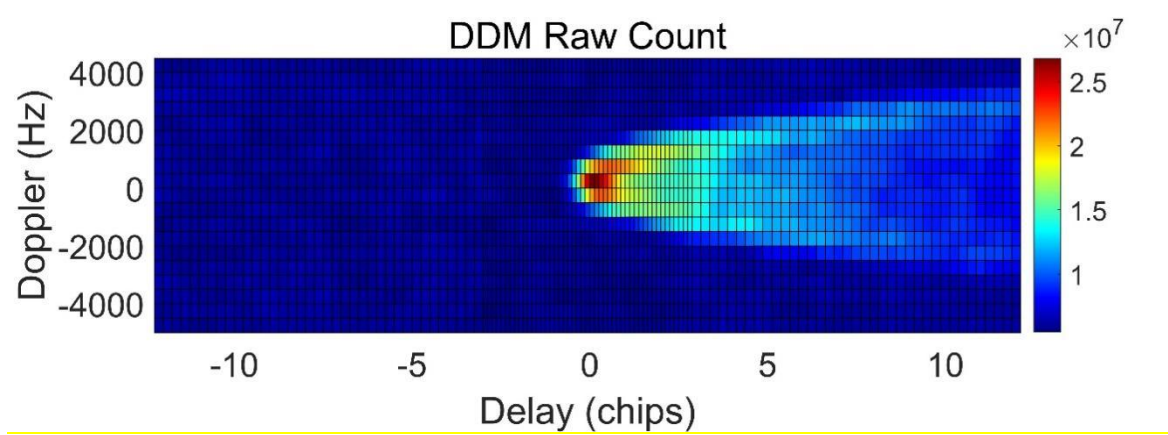


**Figure 2.** FY3E GNOS-R Non-Uniform DDM measurement.

During our analysis, it is assumed that the DDM is dominated by coherent scattering. To calculate surface reflectivity (SR), we use the following equation, which is commonly used in TDS-1 or CYGNSS. We have slightly modified the equation to suit GNOS-R SR[23].

$$\Gamma(\theta) = \frac{(R_r + R_t)^2 (P_{DDM} - N)}{F R_t^2 R_r^2 4\pi} \quad (1)$$

where  $\Gamma$  is the SR,  $R_r$  and  $R_t$  are the distance from the specular points to the receiver and the transmitter, respectively,  $P_{DDM}$  is the peak DDM power,  $N$  refers to noise, and  $F$  is the DDM BRCS-Factor (Bistatic Radar Cross Section Factor)[23],

$$F = \frac{\lambda^2 P_t G_t G_r}{(4\pi)^3 R_t^2 R_r^2} \quad (2)$$

Where  $P_t G_t$  is the GNSS Effective Isotropic Radiated Power (EIRP) and  $G_r$  is the receiver antenna pattern.

Different from the pan-tropical coverage of CYGNSS, FY-3E GNOS-R has the unique ability of almost global coverage (within the latitude range of  $85^{\circ}$ ), It should be mentioned that latitude higher than  $85^{\circ}$  has almost no soil moisture content. Therefore, the global here refers to the coverage of soil moisture on earth. Daily observations on land surfaces are with percentages of 24%. The specular reflection points of FY-3E GNOS-R on a single day (August 10, 2021) are shown in Figure 2. As for GNOS-R, it will have the global coverage about every 15 days. Here, we will employ the first month after GNOS-R was launched for our soil moisture retrieval algorithm estimation.

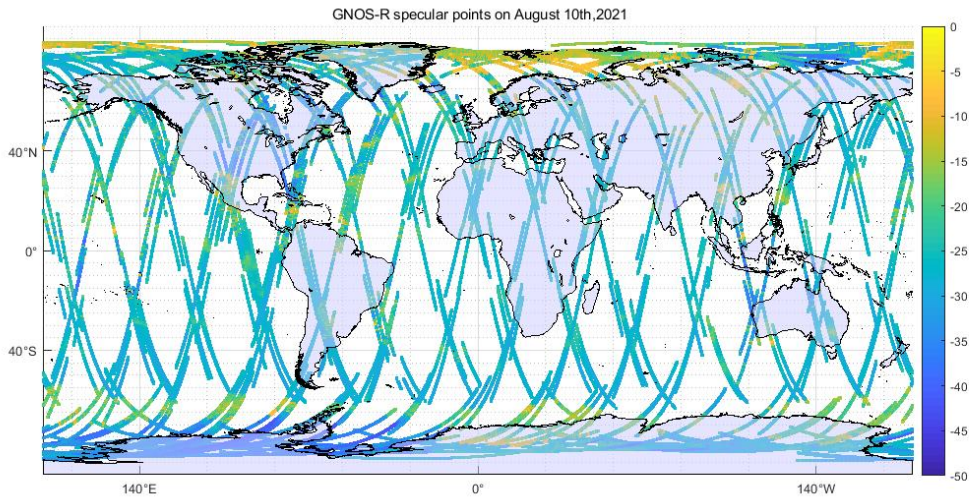


**Figure 3.** Specular reflection points of FY-3E GNOS-R on August 10, 2021, while the colorbar on the right hand indicate the SR of GNOS-R.

## 2.2 Ancillary data from SMAP

The Soil Moisture Active Passive (SMAP) satellite, designed by NASA, was launched on January 31, 2015. Operating in the L-band, the satellite boasts an average revisiting period of 2-3 days. The unique advantage of SMAP is its capability to combine L-band radar and microwave radiometry. This feature enables the acquisition of high-resolution radar data and high-precision microwave radiometry simultaneously[23].

Based on the EASE-grid 2.0, NASA has released three soil moisture products with varying spatial resolutions: (1) High-precision soil moisture product with a resolution of 36 km, solely using SMAP polarization brightness temperature. (2) Low-precision soil water product with a resolution of 3 km, solely retrieved by the SMAP radar backscatter coefficient. (3) Intermediary precision soil moisture product with a resolution of 9 km, which incorporates both active and passive observation data.

NASA has made soil moisture products for SMAP's ascending orbit (6 PM local solar time) and descending orbit (6 AM local solar time) freely available through the National Snow and Ice Data Center (NSIDC). However, the radar component failed in July 2015, and since then, all measurements from the mission have originated solely from the radiometer.

In this study, we utilized the most recent version of the SMAP soil moisture product, known as Level-3 (L3). The most noteworthy change in this version is the replacement of the single channel algorithm (SCA-V) with the dual channel algorithm (DCA) as the baseline algorithm. Additionally, the maximum value of bulk density has been revised from 1 to 2.65.

For our final retrieval, we combined the ascending and descending orbit data from each day. We also incorporated ancillary data for soil characteristics, such as bulk density, clay fraction, and roughness coefficient. To account for the effects of vegetation, we included the vegetation water content (VWC) and opacity. Both VWC and opacity were estimated for the retrieval because we aimed to evaluate their impact on the final retrieval accuracy results.

We will combine the ascending orbit data and descending orbit data of each day for the final retrieval. Other ancillary data are also needed. As for soil, ancillary data such as bulk density, clay fraction, roughness coefficient are employed. Meanwhile, to take the vegetation effects into consideration, vegetation water content (VWC) and opacity  $\tau$  are employed. Both VWC and  $\tau$  are estimated for the retrieval is because that we want to evaluate their accuracy effects for the final retrieval accuracy results.

### **2.3 Land cover and land type classification**

During our analysis, we have employed the MODIS Land Cover Type Product (MCD12Q1), which has a 500m spatial resolution at annual time step. The data covers the entire globe from 2001 to 2020. We have employed the data in Year 2020 because the land cover and land type information are assumed to be the same with the periods employed in our study. Maps of the International Geosphere-Biosphere Programme (IGBP), University of Maryland (UMD), and Leaf Area Index (LAI) classification schemes are provided. There are legends in the 18 MCD12Q1 International Geosphere-Biosphere Programme (IGBP) classification, and the class descriptions can be found from the reference[24]. The land cover and land type information for the global coverage is shown in Figure 4. In order for the final soil moisture retrieval, we have re-classified the IGBP legends to three types as the following table, i.e. barren, low-vegetation and forest. In other words, we will utilize three types of retrieval algorithms that are tailored to the aforementioned three categories of land cover, while the detailed information is presented in Table 1.

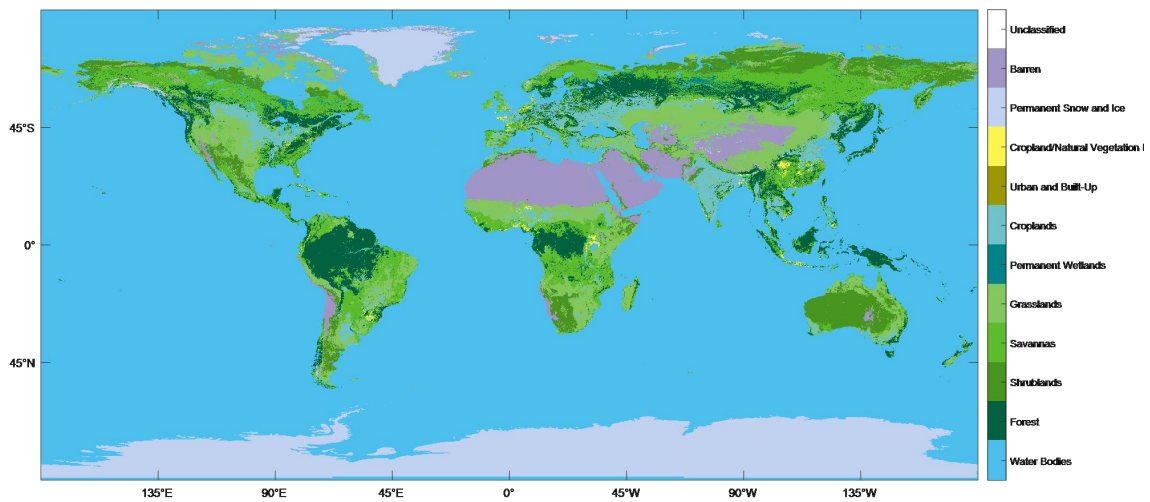


**Figure 4.** global land cover and land use map

**Table 1: MCD12Q1 International Geosphere-Biosphere Program (IGBP) legend and re-classified land cover types**

Name	Value	New classifications
Evergreen Needleleaf Forests	1	Forest
Evergreen Broadleaf Forests	2	Forest
Deciduous Needleleaf Forests	3	Forest
Deciduous Broadleaf Forests	4	Forest
Mixed Forests	5	Forest
Closed Shrublands	6	Forest
Open Shrublands	7	Low-Vegetation
Woody Savannas	8	Low-Vegetation
Savannas	9	Low-Vegetation
Grasslands	10	Low-Vegetation
Permanent Wetlands	11	Low-Vegetation
Croplands	12	Low-Vegetation
Urban and Built-up Lands	13	Abandoned-type
Cropland/Natural Vegetation Mosaics	14	Low-Vegetation
Permanent Snow and Ice	15	Abandoned-type
Barren	16	Barren
Water Bodies	17	Abandoned-type
Unclassified	255	Abandoned-type

### 3. Methodology (Design/Approach)

This section presents a comprehensive overview of the theoretical underpinnings and methodology employed in our GNOS-R soil moisture estimation process. It includes simulations that illustrate the formulas and demonstrate the principles behind our analysis and algorithms.

#### 3.1 Bare soil formula and simulations

In the context of bare soil conditions, surface roughness significantly influences the final soil reflectivity. The surface reflectivity (SR) of bare soil can be modeled using Equation (3)[25]:

$$SR(\theta) = \Re^2(\theta) \exp(-4k^2 s^2 \cos^2(\theta)) \quad (3)$$

where, SR is a function of incidence angle  $\theta$ ,  $k$  is the signal wavenumber and  $s$  is the surface -root-mean squared height, presents the surface roughness conditions.  $\Re$  is the Fresnel reflection coefficient, as for the LR polarization of GNOS-R,  $\Re$  can be modeled as the linear combination of reflectivity at horizontal and vertical polarization using the following equations (4-6)[3,25]:

$$\Re(\theta) = \left| \frac{\Re_v(\theta) - \Re_h(\theta)}{2} \right|^2 \quad (4)$$

$$\Re_v(\epsilon_r, \theta) = \frac{\epsilon_r \cos \theta_i - \sqrt{\epsilon_r - \sin^2 \theta}}{\epsilon_r \cos \theta_i + \sqrt{\epsilon_r - \sin^2 \theta}} \quad (5)$$

$$\Re_h(\epsilon_r, \theta) = \frac{\cos \theta_i - \sqrt{\epsilon_r - \sin^2 \theta}}{\cos \theta_i + \sqrt{\epsilon_r - \sin^2 \theta}} \quad (6)$$

$\epsilon_r$  is the dielectric constants.  $\Re_v$  and  $\Re_h$  are the Fresnel reflectivity at vertical and horizontal polarizations, respectively.

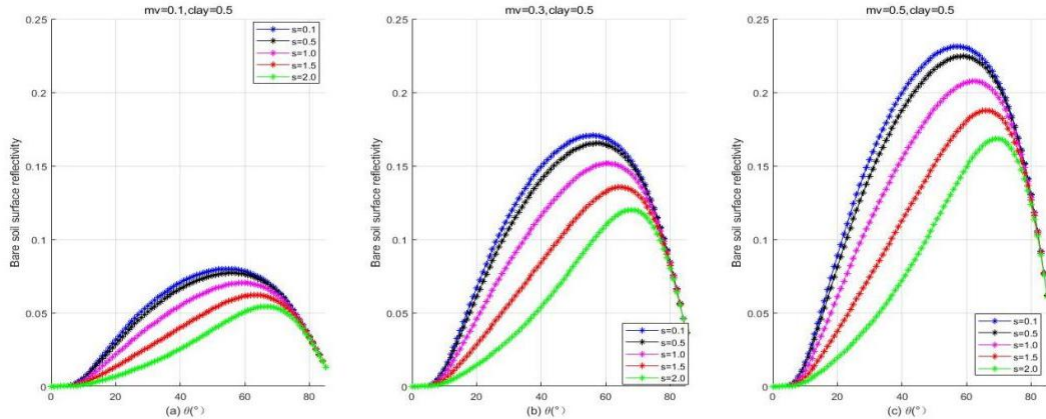


Figure 6. Relationship between bare soil surface reflectivity and specular incidence angle. The lines with different colors represent different surface roughness conditions, as indicated in the legend. The surface root-mean-squared height is denoted by "s". The volumetric soil moisture content in subfigures (a), (b), and (c) are 0.1, 0.3, and 0.5, respectively. The clay fraction for both conditions is 50%.

Figure 6 illustrates the relationship between bare soil surface reflectivity and specular incidence angles. The volumetric soil moisture content in subfigures (a), (b), and (c) is 0.1, 0.3, and 0.5, respectively. As expected, as the soil moisture content increases, the bare soil surface reflectivity calculated using Equations 1-4 also increases. Different colored lines represent various surface roughness conditions, indicated by the root mean squared height (s). As the incidence angle increases, the surface reflectivity for bare soil shows a decreasing trend for larger incidence angles, typically between  $60^\circ$  to  $80^\circ$ . During these incidence angle ranges, different roughness conditions have minimal effects on the surface reflectivity. However, as surface roughness increases ( $s=1.0$ ,  $s=1.5$ ,  $s=2.0$ ), the surface reflectivity increases with the incidence angles ( $0^\circ \leq \theta \leq 60^\circ$ ). This trend becomes more pronounced for larger root-mean-squared heights. Therefore, the final surface reflectivity of bare soil is influenced by both specular incidence angles and surface roughness, with the degree of this influence varying depending on the specific conditions.

The SMAP roughness coefficients cannot be used directly for the final retrieval in GNSS-R, as it operates in a bistatic scattering radar system with forward scattering mode. The working mode of SMAP radiometer is suitable for passive emissivity and its microwave physical mechanism is completely different from that of GNSS-R. Therefore, we propose two formulas (Case 1 in Equation 7 and Case 2 in Equation 8) to correct the surface roughness information obtained from GNOS-R observations. It should be noted that the distinction between Equations 7 and 8 lies in the representation of cosine, with the former involving squaring and the latter not.

$$\text{Case 1: } SR(\theta) = R^2(\theta) \exp(C1 * \cos^2(\theta)) \quad (7)$$

$$\text{Case 2: } SR(\theta) = R^2(\theta) \exp(C2 * \cos(\theta)) \quad (8)$$

Using the above two formulas, we can obtain the regression coefficients C1 and C2. Then, the corresponding surface roughness coefficients of GNOS-R can be calculated as follows:

$$s_1 = \sqrt{-\frac{C1}{4k^2}} \quad (9)$$

$$s_2 = -\frac{C2}{2k} \quad (10)$$

### 3.2 Vegetation formula and simulations

In regions with vegetation cover, signal attenuation due to the vegetation can impact soil moisture retrieval accuracy. We have incorporated both zero-order and first-order vegetation scattering models to account for these effects. Figure 7 presents the schematic of GNSS-R reflection from the three-layer model (air layer, vegetation layer, and soil layer). Figure 7a illustrates the zero-order model, and Figure 7b depicts the first-order model, which includes volume scattering. The soil layer is depicted with a curved interface to represent surface roughness conditions.

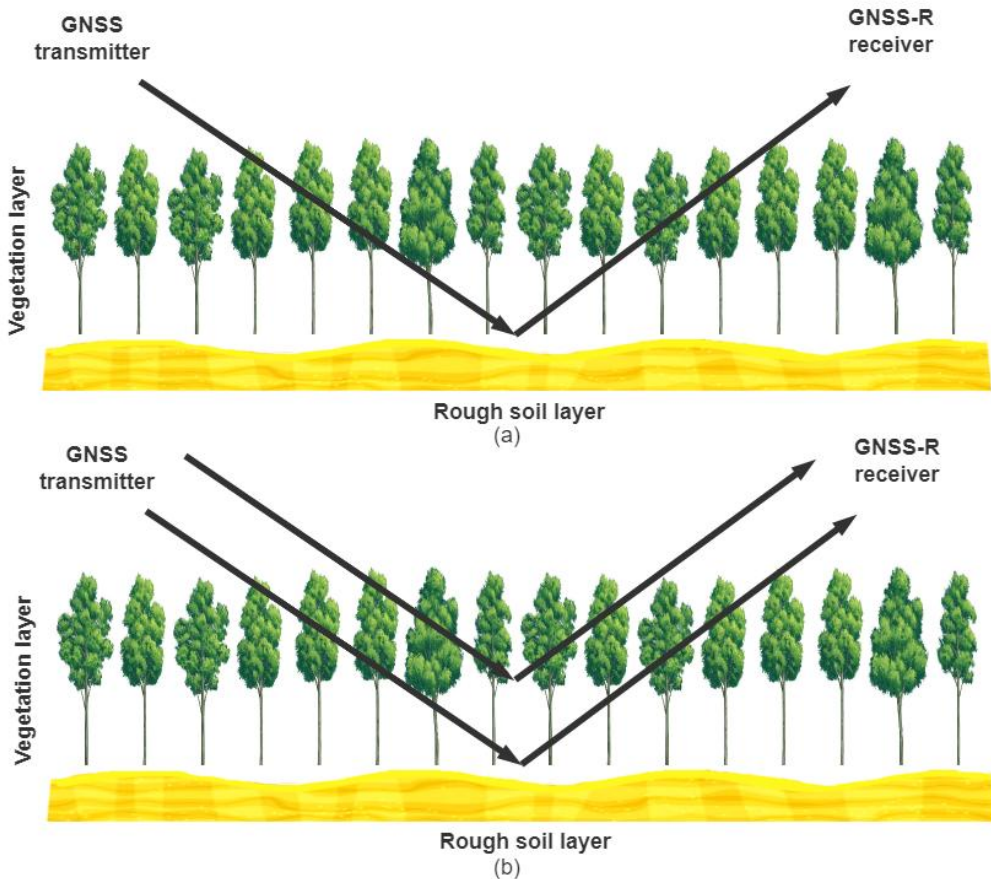


**Figure 7.** Illustration of zero-order model(a) and first-order model(b)

Under zero-order conditions, GNSS signals attenuate the vegetation layer from both the incident and reflection directions as shown in Figure 7a. The formula for a zero-order model is as follows [25]:

$$SR(\theta) = \Re^2(\theta) \gamma^2 \exp(-4k^2 s^2 \cos^2(\theta)) \quad (11)$$

$$\gamma(\theta) = \exp(-\tau * \csc(\theta)) \quad (12)$$

Where the transmissivity  $\gamma$  accounts for the attenuation of signal propagation by vegetation layer and it can be presented by the exponential term for vegetation opacity  $\tau$  and incidence angles  $\theta$  (Eq.12). Figure 8a demonstrates that as the incidence angle ( $\theta$ ) increases, the transmissivity ( $\tau$ ) increases.

The decrease in transmissivity ( $\tau$ ) is also apparent as the vegetation opacity ( $\tau$ ) increases. The trend of  $\tau$  versus  $\theta$  remains almost constant for incidence angles between  $30^\circ$  and  $80^\circ$ . However, for incidence angles lower than  $30^\circ$ , the increasing trend of  $\tau$  becomes more pronounced.

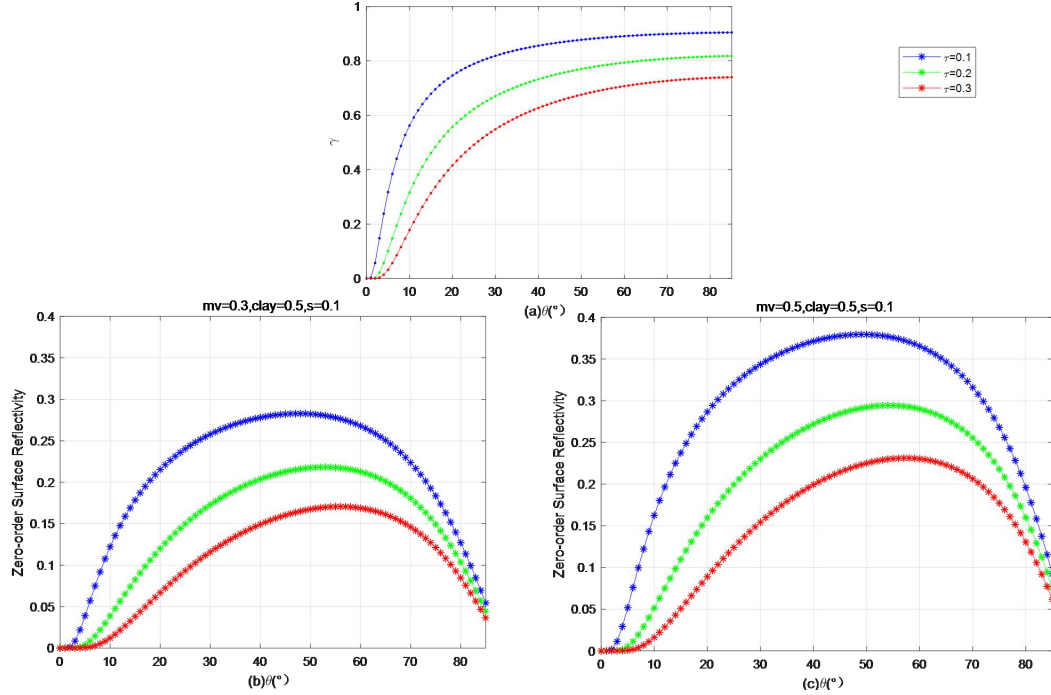


**Figure 8** Scattering features of zero-order model: transmissivity (a) and surface reflectivity versus the specular incidence angles(b,c); while the soil clay fraction and s for both figure b and c are 0.5 and 0.1, respectively. and the soil moisture content for figure b is 0.3, while the one for figure c is 0.5.

The main difference between Figure 8b and Figure 8c lies in the soil moisture content, with the former having a volumetric soil moisture content of 0.3 and the latter having a value of 0.5. However, both figures show that surface reflectivity calculated using a zero-order model model(Equation 11 and 12) has almost the same trend with respect to incidence angles, but with different amplitudes. Specifically, higher soil moisture contents result in higher surface reflectivities under corresponding conditions. If the soil moisture content is fixed, then higher vegetation opacity  $\tau$  will result in lower surface reflectivity due to increased attenuation. Conversely, if both soil moisture content and vegetation

opacity  $\tau$  are fixed, then surface reflectivity will increase as the incidence angle (between  $0^\circ$  and  $45^\circ$ ) increases. However, when the incidence angle is lower than  $45^\circ$ , the trend is reversed.

The first-order model, as depicted in Figure 7b, accounts for vegetation volume scattering, which is not considered in the zero-order model and the volume scattering term occurs in the vegetation layer.

The formulas for the first-order model are as follows [26]:

$$SR(\theta) = SR_{veg} + \gamma^2 SR_{soil} \quad (13)$$

$$\gamma^2(\theta) = \exp(-2 * B * \tau * \csc(\theta)) \quad (14)$$

$$SR_{veg}(\theta) = A * \tau * \sin(\theta) * (1 - \gamma^2) \quad (15)$$

The volume scattering term  $SR_{veg}$  is depicted in Equation 15, while Equation 14 gives the formula to calculate the transmissivity  $\gamma$ . The total surface reflectivity  $SR$  is calculated by Equation 13.  $SR_{soil}$  is the surface reflectivity of bare soil and it can be calculated as presented in Equation 7 and 8. It should be mentioned that  $\tau$  is the vegetation optical that is achieved by SMAP products, however, we still believe that this parameter directly achieved from SMAP product cannot be utilized in GNOS-R soil moisture retrieval, the reason is somewhat the same with that of the bare soil, that is to say, the microwave physical mechanisms for them are not the same and we need to employ parameters to correct this information, therefore, coefficients A and B are employed.

With the consideration of the volume scattering as depicted in the first-order model, we employ it to perform simulations demonstrating the effect of specular incidence angles on vegetation scattering properties.

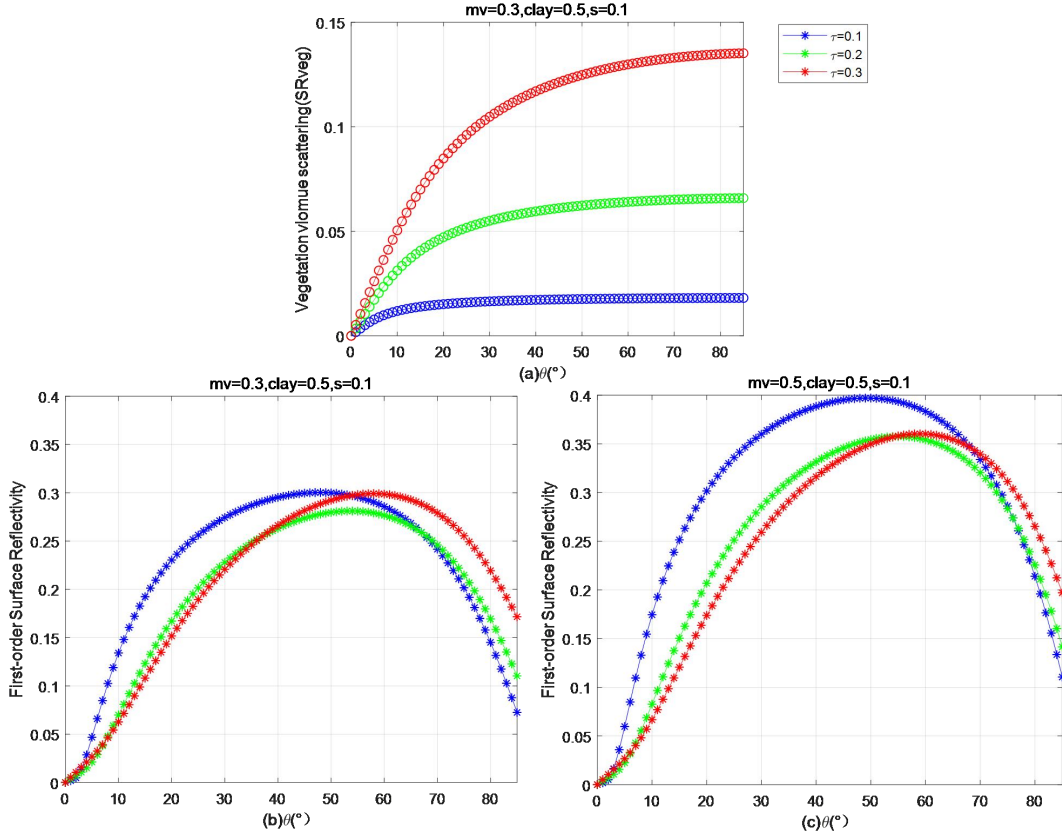


Figure 9. Scattering features of first-order model. The vegetation volumes scattering reflectivity as shown in Equation 6 is shown in figure a. while the total surface reflectivity are presented in figure b and c and the clay fraction and s are 0.5 and 0.1 for, respectively. while the soil moisture content for figure b is 0.3, and the one for figure c is 0.5.

As shown in Figure 9a, vegetation volume scattering ( $SR_{veg}$ ) increases as the specular incidence angles increase. This phenomenon is particularly evident when the incidence angle is lower than  $30^\circ$ , after which the vegetation volume scattering becomes constant and has almost no relationship with the incidence angle. When  $\tau$  is fixed,  $SR_{veg}$  also increases as  $\tau$  increases. The surface reflectivity for two types of soil moisture content is highly related to vegetation opacity ( $\tau$ ) and the specular incidence angle. Specifically, when the incidence angle is lower than  $40^\circ$ , surface reflectivity increases as the incidence angle increases. However, it decreases as the incidence angles (higher than  $50^\circ$ ) increase.

As illustrated in Figures 8 and 9, the simulations of surface reflectivity for both zero-order and first-order models exhibit a strong dependence on incidence angles. Therefore, it is essential to carefully consider these angles when attempting to retrieve soil moisture information. The surface reflectivity calculated using the zero-order model and the first-order model differ somewhat due to the effects of volume scattering, which are accounted for in the first-order model. Given that the frequency band of

GNSS-R is L band, where vegetation volume scattering cannot be ignored, we will utilize the formulas of the first-order model (Equations 13 to 15) for subsequent soil moisture retrieval.

### 3.3 Soil moisture retrieval algorithms

Based on different land cover type, we adopted different soil moisture retrieval methods. While the flowchart of our work is shown in Figure 10. From the GNOS-R data, we use equations 1 and 6 to get the surface reflectivity. Ancillary data include SMAP and the IGBP data. From the IGBP data, we can classify the land cover type into three categories, i.e., barren soil, low vegetation, and high forest. As for the barren soil, we will base on equations 7 -10 to get a surface roughness correction coefficient. Then the surface roughness coefficients related to GNOS-R is achieved, by which we can get rid of the effects of surface roughness. The pure Fresnel reflectivity is gotten and the corresponding soil moisture content is achieved by the database built based on the dielectric constant model. As for vegetation covered soil ground, we employed the first order model (Equations 13 to 15) and by combining the SMAP vegetation parameters, such as VWC and  $\tau$ , we get the regression coefficients, by which we can get the terms of vegetation attenuation and vegetation volume scattering. After get rid of these two terms, we can remove the effects of vegetation. Then by taking the surface roughness effects into consideration(Equation 7 to 10), we can remove the surface roughness effects and with the same method as barren soil, we can get the retrieved soil moisture contents. The flowchart for our soil moisture retrieval algorithms are presented in Figure 10.

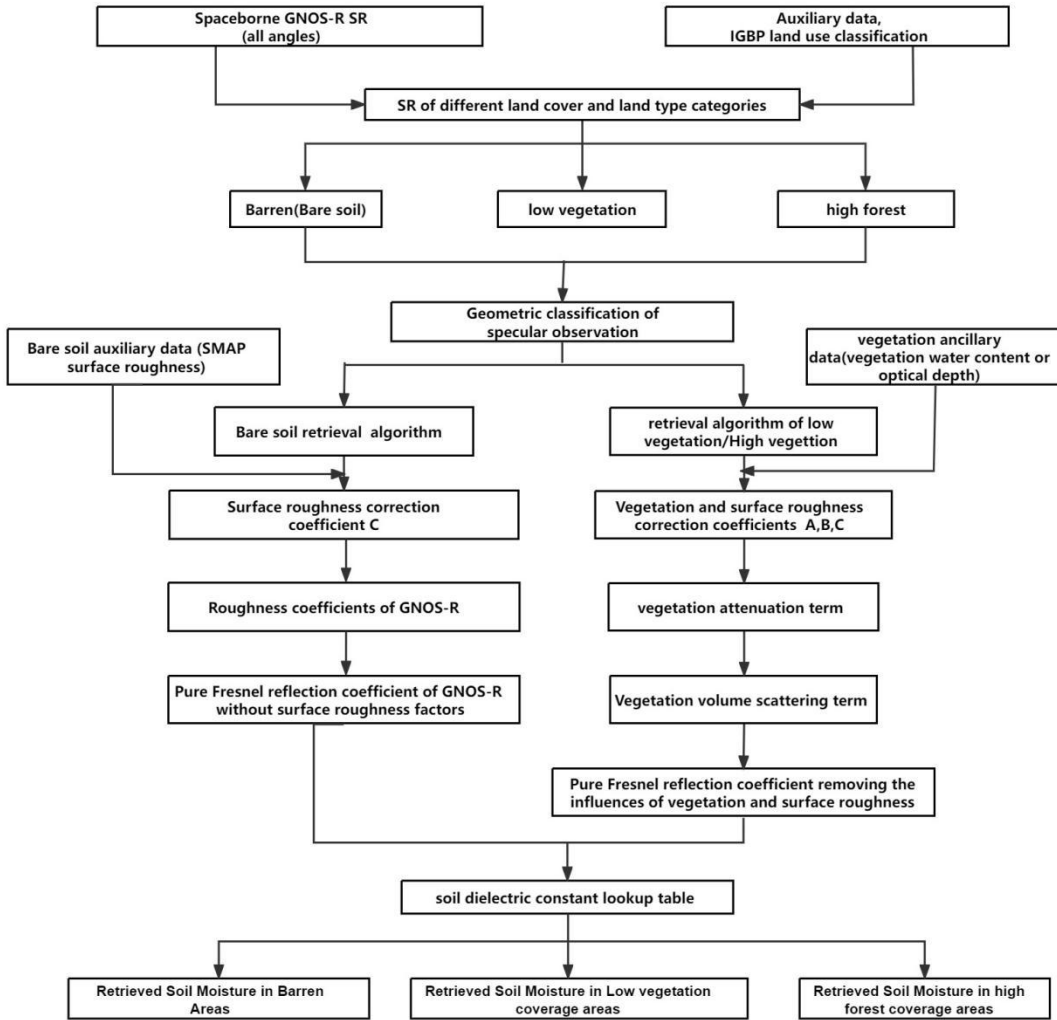


**Figure 10** Flowchart for FY-3E GNOS-R soil moisture retrieval

## 4. Results

### 4.1 Performance of SM retrieval for barren land type

In most current research on GNSS-R soil moisture inversion, the roughness coefficient from SMAP is directly used for correction. However, it is important to note that the roughness coefficient of SMAP represents surface roughness observed in back-scattering direction, while GNSS-R has a forward scattering characteristic. This means that the observation mechanisms of these two techniques are significantly different. Therefore, in our work, we will re-evaluate and estimate the SMAP roughness coefficient. The equations presented in equations 7 and 8 will be used to correct the corresponding GNSS-R surface roughness information. Specifically, the method to obtain the GNSS-R roughness

coefficient involves first calculating the regression coefficients C1 and C2 using Formula 7 and Formula 8. Then, the corresponding GNSS-R roughness coefficient is obtained using equations 9 and 10.

The calculated coefficients C1 and C2, whose values are between -10 and 0. As for case 1, GNOS-R roughness coefficient is between 0 to 6, while for Case 2, the roughness coefficient is between 0 to 15. The coefficient of Case 1 seems a little lower than that of Case 2. The reasons for that are the roughness coefficient for both cases as presented in Equation 7 and 8 are very different. this is caused by the form of  $\theta$ , for Case 1, we employ  $\cos^2(\theta)$  to take the incidence angles into consideration, while for Case 2, we change the form to  $\cos(\theta)$ .

Now, we will take the incidence angles  $\theta$  into considerations by dividing the incidence angles  $\theta$  every  $10^\circ$ . The calculated results are shown in Figure 11.

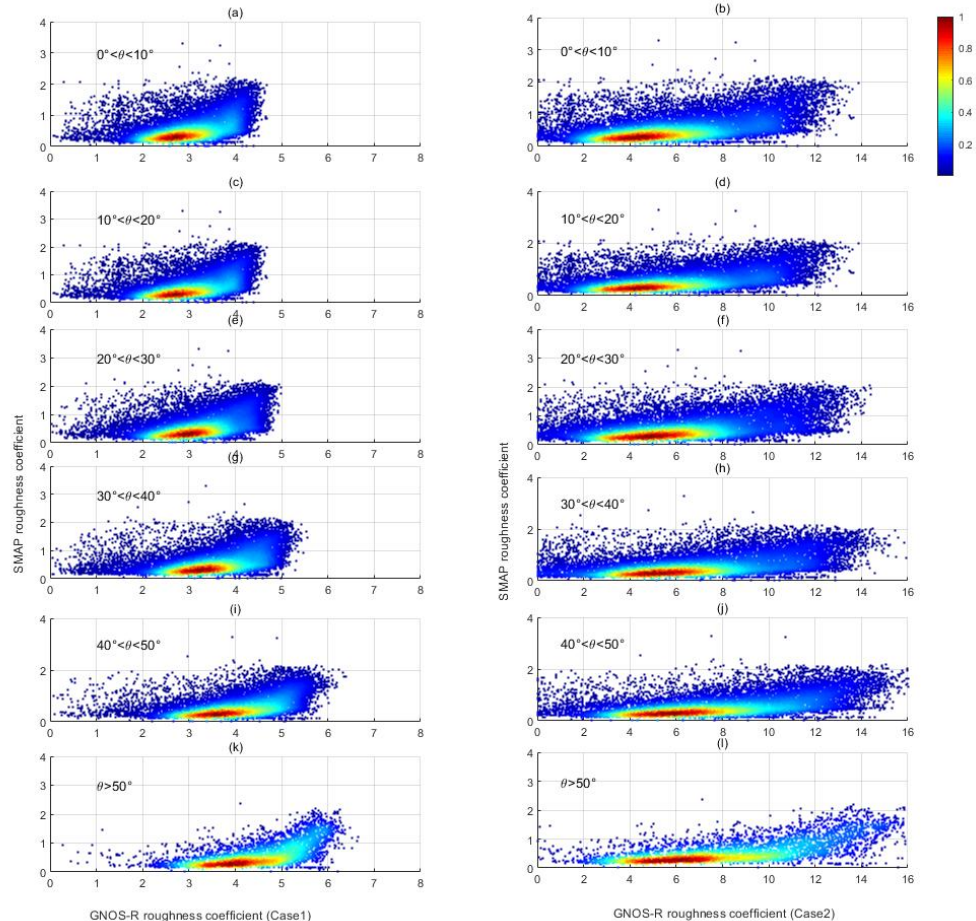


Figure 11. Comparisons between SMAP roughness coefficients and the ones of GNOS-R for different incidence angles  $\theta$

The roughness coefficients for GNOS-R vary with observation geometry, specifically the specular incidence angle. This is because the surface roughness conditions are different at different observation angles. In other words, the same observation target can have different roughness conditions depending on the observation geometry. Table 1 provides a summary of GNOS-R roughness coefficients for different observation geometries. For Case 1, as the incidence angle increases, the minimum value of the GNOS-R surface roughness coefficient changes from 1.4 to 3, while the maximum value ranges from 4 to 5.5. For Case 2, the minimum value increases from 1.5 to 4 as the incidence angle changes, while the maximum value changes from 11 to 14.1. The roughness coefficients vary significantly every  $10^\circ$ . More detailed values are shown in Table 1.

Table 2. GNOS-R surface roughness coefficients for different observation geometry of two cases.

Observation geometry $\theta$	Case 1	Case 2
$0^\circ\text{-}10^\circ$	1.4-4	1.5-11
$11^\circ\text{-}20^\circ$	2.1-4.5	2.1-12
$21^\circ\text{-}30^\circ$	2.2-4.8	2.2-13
$31^\circ\text{-}40^\circ$	2.2-5.5	2.2-14
$41^\circ\text{-}50^\circ$	2.5-5.5	2.5-14.5
$>50^\circ$	3-5.5	4-14.1

After corrections of the GNOS-R surface soil roughness in different specular incidence angles range, we can get the soil moisture content and the corresponding retrieval results are presented in Figure 14. The left column is for Case 1 and the right column is for Case 2. The first row to the sixth row are for different incidence angles, which are separated by every  $10^\circ$ .

With the method presented in this paper, the soil moisture retrieval accuracy for Case 1 and Case 2 are described in Table 3 and the RMSE for both cases within  $10^\circ$  incidence angle interval are illustrated in Table 3 in detail and the final RMSE with the combination of the incidence angles are 0.0235 and 0.0224, respectively.

Table 3. Soil moisture retrieval accuracy of RSME

Incidence angles $\theta$	RMSE(Case1)	RMSE(Case 2)
$0^\circ\text{-}10^\circ$	0.0061	0.0057
$11^\circ\text{-}20^\circ$	0.0259	0.0252
$21^\circ\text{-}30^\circ$	0.0245	0.0205
$31^\circ\text{-}40^\circ$	0.0214	0.0161
$41^\circ\text{-}50^\circ$	0.0180	0.0111
$>50^\circ$	0.0055	0.0048

Combination Considerations of incidence angles separation	0.0235	0.0224
---	--------	--------

## 4.2 Soil moisture retrieval in low vegetation coverage areas

The basic formula used for vegetation covered soil moisture is already presented in Equations 13 to 15.

While in this section, we will evaluate the different SMAP vegetation parameters such as VWC and  $\tau$  for the final retrieval accuracy based on Equations 13 to 15.

In Equation 14, we know B is related to two-way propagation path and researchers have used a constant ( $B=0.091$ ), which explores the value in backscattering case for CYGNSS soil moisture estimation. However, we will re-calculate the B parameters( $B1$  and  $B2$ ) in each of the GNOS-R grid according to the specular incidence angle information for our algorithm, since we believe the value in backscattering case may not be directly used for GNOS-R, the reasons are that the scattering mechanisms for these two cases are totally different. As for  $\gamma^2$ , two cases are evaluated here. For Case 1, we will use VWC and for the second case we will use  $\tau$ .

$$\text{Case1: } \gamma_1^2 = \exp(B1 * (-2 * VWC * \csc(\theta))) \quad (16)$$

$$\text{Case2: } \gamma_2^2 = \exp(B2 * (-2 * \tau * \csc(\theta))) \quad (17)$$

In Equation 15, parameter A is related to vegetation density. While if A is multiple with the vegetation parameters, such as the VWC or  $\tau$  achieved from SMAP, then it will become the volume scattering term from vegetation. A fixed constant for parameter A ( $A=0.0012$ ) is used in the previous paper. However, we will re-calculate this parameter in each GNOS-R grid due to the same reasons as mentioned for parameter B. Also, two cases are evaluated here. The detail information is like the following:

$$\text{Case1: } SR_{veg} = A1 * VWC * \sin(\theta) * (1 - \gamma^2) \quad (18)$$

$$\text{Case2: } SR_{veg} = A2 * \tau * \sin(\theta) * (1 - \gamma^2) \quad (19)$$

While as for parameter C, two cases are also employed for the final soil moisture retrieval. The formulas are like the following.

$$\text{Case1: } SR_{soil} = \Re(\theta)^2 * \exp(-C1 * h^2 * \cos^2(\theta)) \quad (20)$$

$$\text{Case2: } SR_{soil} = \Re(\theta)^2 * \exp(-C2 * h * \cos(\theta)) \quad (21)$$

While C1 and C2 are used to correct the surface roughness effects and the reasons why not used the SMAP surface roughness coefficient is the same as for parameter A and B.

To summarize, the total surface reflectivity to calculate the effects of both surface roughness and vegetation can be get the following four cases.

$$\text{Case1: } SR = \gamma_1^2 * \Re(\theta)^2 * \exp(-C1 * h^2 * \cos^2(\theta)) + A1 * VWC * \sin(\theta) * (1 - \gamma_1^2) \quad (22)$$

$$\text{Case2: } SR = \gamma_2^2 * \Re(\theta)^2 * \exp(-C2 * h^2 * \cos^2(\theta)) + A2 * \tau * \sin(\theta) * (1 - \gamma_2^2) \quad (23)$$

$$\text{Case3: } SR = \gamma_3^2 * \Re(\theta)^2 * \exp(-C3 * h * \cos(\theta)) + A3 * VWC * \sin(\theta) * (1 - \gamma_3^2) \quad (24)$$

$$\text{Case4: } SR = \gamma_4^2 * \Re(\theta)^2 * \exp(-C4 * h * \cos(\theta)) + A4 * \tau * \sin(\theta) * (1 - \gamma_4^2) \quad (25)$$

Figure 12 gives the distribution of coefficient A for four cases as presented in Equation 22 to 25, while as for Case 1 and Case 3 , the vegetation inputs parameter calculated from SMAP are VWC, while the ones for Case 2 and Case 4 are  $\tau$  . The roughness correction methods for Case 1 and Case 2 are  $h^2$  , while the ones for Case 3 and Case 4 are  $h$  . The primary differences between the four cases lie in the use of vegetation input parameters from SMAP and the methods for roughness correction, which depend on the cosine of the angle of incidence. In other words, it is related to the correction of the incidence angle. It is important to note that the correction parameter A is used to adjust the values of vegetation density. This is because the previously mentioned vegetation density, as demonstrated in the equations for the backscattering radar equation formulas, cannot be directly applied in GNSS-R bistatic forward scattering scenarios. The vegetation density correction parameter A ranges from -0.1 to 0.12 for Case 1, -0.8 to 1.88 for Case 2, -0.2 to 0.12 and -0.9 to 0.82 for the other two cases, respectively. The dynamic ranges of Parameter A for these four cases are 0.22, 2.68, 0.14, and 1.72 respectively. This means that if we want to correct the corresponding information as shown in the equations for the above four cases, the maximum dynamic range is for Case 2, followed by Case 4, then Case 1 and Case 3.

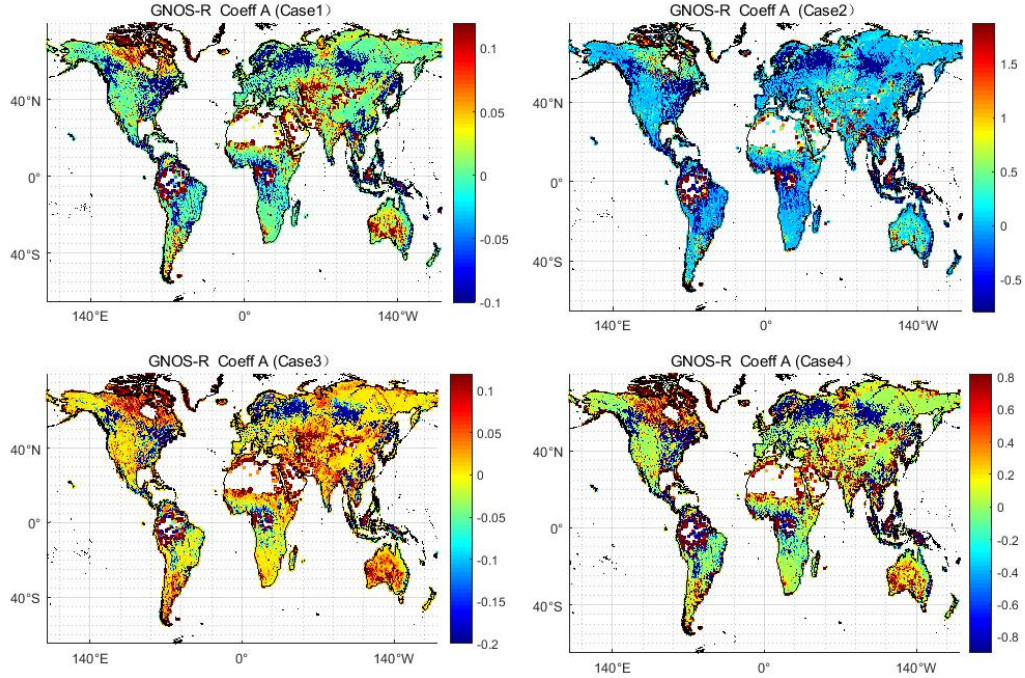


Figure 12. Values of vegetation density correction parameter A for four cases.

The two-way propagation path correction parameter B is depicted in Figure 13. For Case 1, the B value ranges from 0 to 1, while for Case 2, it ranges from 0 to 7. As mentioned in Equations 16 and 17, the difference between the two correction coefficients B lies in the vegetation input parameters. In Case 1, we used VWC to represent the vegetation parameters, and the coefficient B used to correct the two-way propagation path was between 0 and 1. However, in Case 2, the vegetation information is represented by  $\tau$ , and the coefficient B ranges from 0 to 7. In other words, if we use different vegetation parameters such as VWC and  $\tau$ , there will be a significant difference in the correction coefficients of the two-way propagation path correction parameter. This is because VWC is a parameter that can be used to calculate . It should be noted that although the distribution of different colors for the two cases is almost the same, the values are not identical. Although this section focuses on low vegetation land cover types, there are actually eight different types of low vegetation land cover, which are listed in Table 1. The land cover and land types for the two cases being discussed are shown in Figure 13.

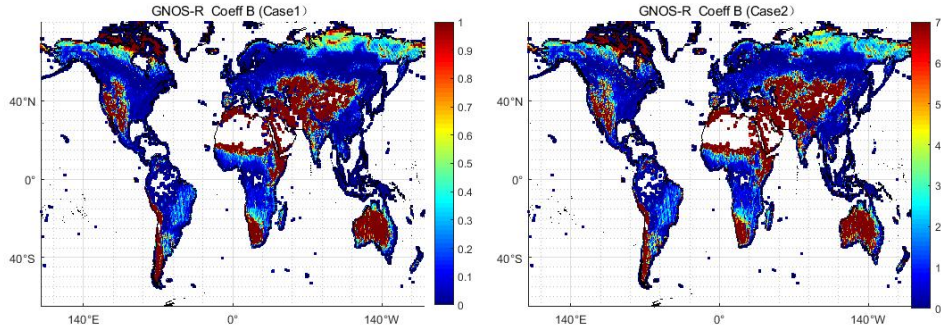


Figure 13. Values of two-way propagation path correction parameter B for four cases

We are aware that the coefficient C is used to adjust the surface roughness information. It is evident that the differences between the two methods lie in their approaches to correcting roughness formation, specifically  $h^2$ , h, and the formation of cosine  $\theta$ . As demonstrated in Equations 22 to 25, the surface reflection of bare soil constitutes a component of the ultimate SR. Therefore, the final correction coefficients for roughness encompass four values: C1, C2, C3, and C4, which correspond to the four scenarios depicted in Equations 22 to 25. The surface roughness correction parameter C is shown in Figure 14. The value ranges for the four cases are -15 to 20, -13 to 60, -30 to 65, and -30 to 63, respectively.

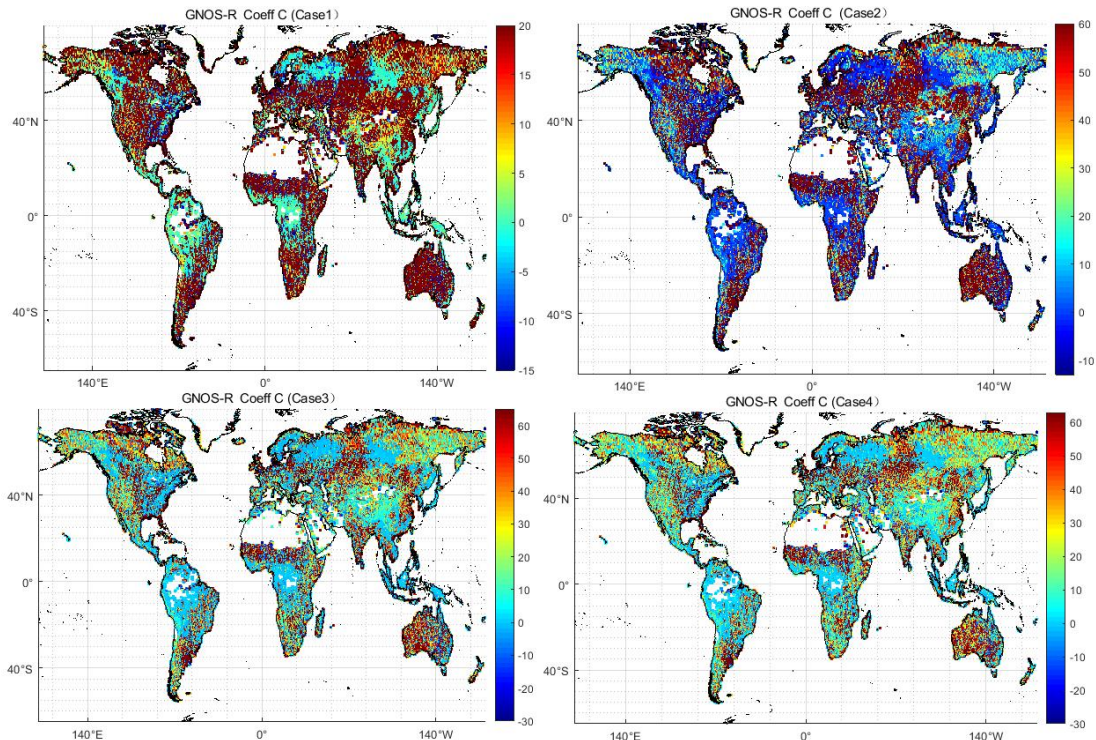


Figure 14. Values of surface roughness correction parameter C for four cases.

With the same method as for barren land coverage areas, we divide the incidence angles with a division of  $10^\circ$ . The RMSE for them is presented in Table 4.

Table 4. RMSE for low vegetation coverage areas

Incidence angles $\theta$	Case1	Case2	Case3	Case4
$0^\circ\text{-}10^\circ$	0.0361	0.0447	0.0336	0.0440
$11^\circ\text{-}20^\circ$	0.0358	0.0390	0.0390	0.0410
$21^\circ\text{-}30^\circ$	0.0359	0.0330	0.0332	0.0331
$31^\circ\text{-}40^\circ$	0.0332	0.0300	0.0307	0.0283
$41^\circ\text{-}50^\circ$	0.0300	0.0261	0.0379	0.0340
$>50^\circ$	0.0470	0.0301	0.0306	0.0310
Combination Considerations of incidence angles separation	0.0296	0.0290	0.0305	0.0316

If we do not consider the incidence angle, the RMSE for Case 1 and 2 is 0.0973 and 0.0558, respectively. However, if we divide the incidence angle into every  $10^\circ$ , the soil moisture retrieval accuracy will increase significantly, with an RMSE ranging from 0.025 to 0.047, and it decreases as the incidence angle increases. After combining all the incidence angles, the final soil moisture retrieval accuracy for Case 1 and Case 2 has an RMSE of 0.0235 and 0.0224, respectively.

#### 4.3 Soil moisture retrieval for high forest coverage areas

For high forest coverage areas, we also use the method mentioned in Section 3.2. In other words, when it comes to high forest coverage areas, we need to use coefficient A to adjust the forest density information. This can be achieved through Equations 22-25, which are the same as those used for low-vegetation coverage areas. The distribution of coefficients A for the four cases is provided in the following figure. For Case 1, the range is between -0.08 and 0.18, while for Case 2, it is between -1.0 and 2.0. The correction coefficients for Case 3 and 4 are from -0.2 to 0.20 and from -0.5 to 1.0, respectively. Generally, the correction coefficients for these four cases do not exceed 2, and the values for each case are quite similar to those of the low-vegetation condition, with some minor differences.

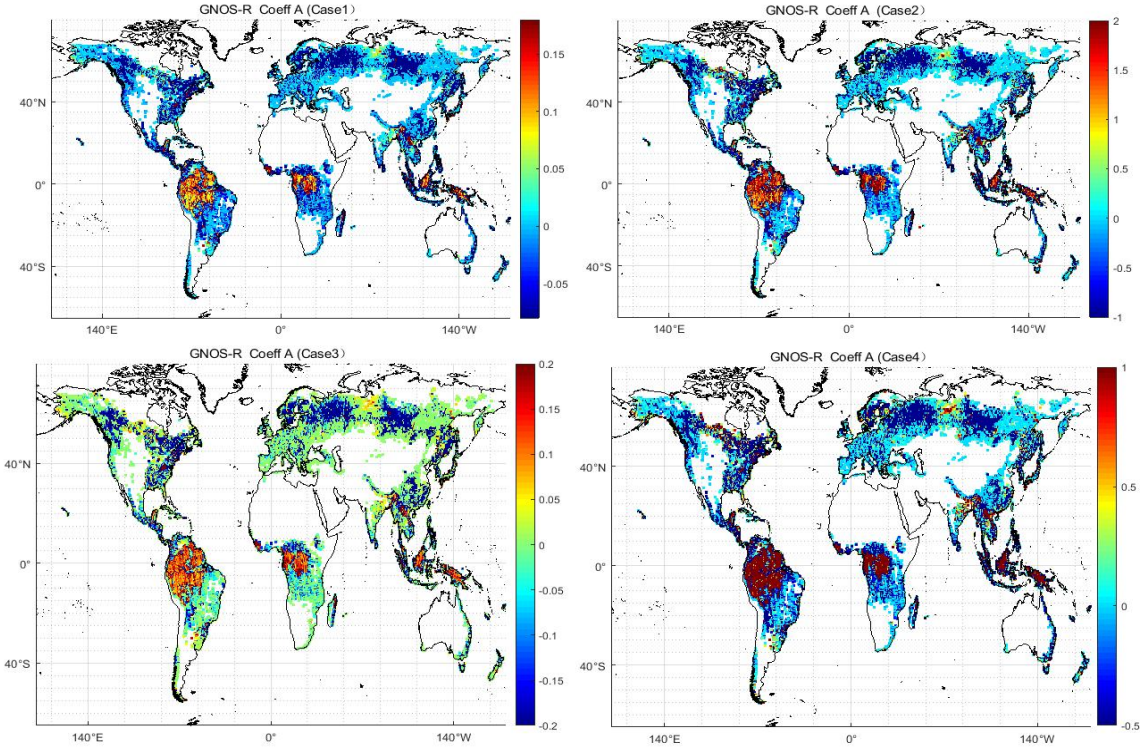


Figure 15. Forest density correction coefficient (A)

The coefficients B used to correct the two-way propagation path information are shown in Figure 16.

For Case 1, this parameter ranges from 0 to 0.18, while for Case 2, it ranges from 0 to 0.9. These values are significantly different from those of the low vegetation condition mentioned earlier, which range from 0 to 1, and the other condition, which ranges from 0 to 7. Therefore, it is important to note that the coefficients B employed to correct the information of the two-way propagation path depend heavily on the land surface type. For low vegetation coverage areas and high forest coverage areas, the corresponding correction information should be used for the final retrieval.

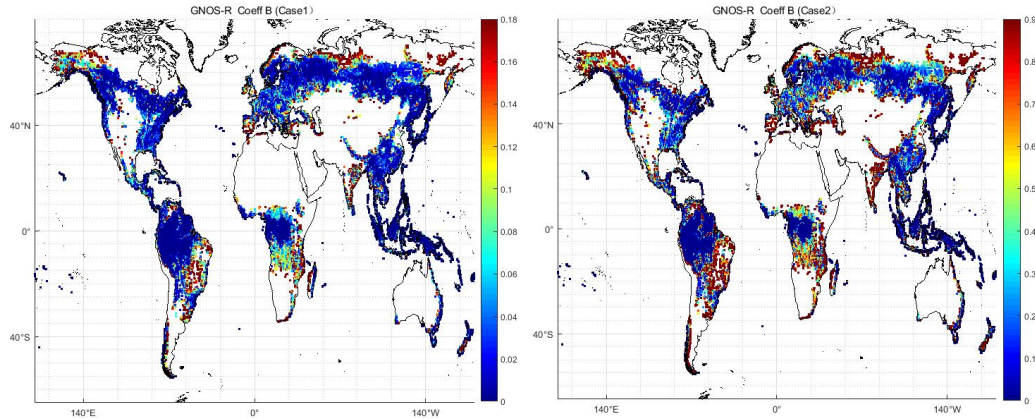


Figure 16 Two-way propagation path correction parameter B

The roughness correction coefficients C for four cases are shown in Figure 17 and they have some differences compared to those of low vegetation coverage areas. For high forest coverage areas, C ranges from -25 to 35 for Case 1, while this value ranges from -33 to 60 for Case 2 and -30 to 135 for Case 3. The coefficient values for Case 4 range from -20 to 93.

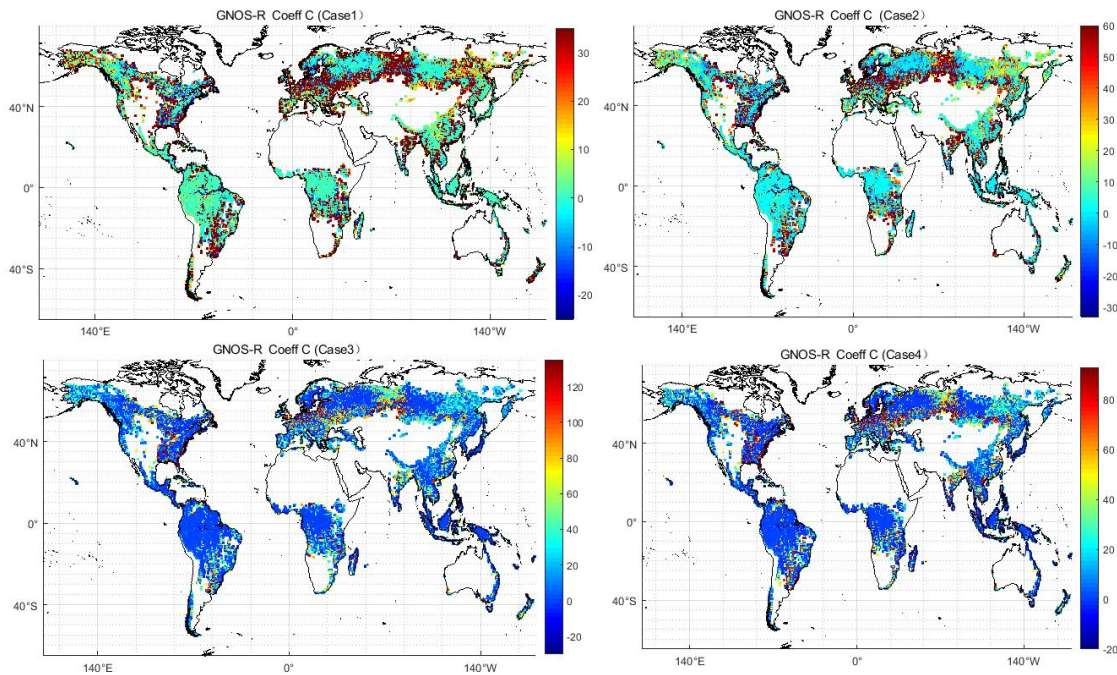


Figure 17 roughness correction coefficients C for four cases

By taking into account the incidence angles and dividing them into  $10^\circ$  intervals, the soil moisture retrieval accuracy improved significantly. The detailed information is shown in Table 5. The final soil moisture retrieval accuracies for the four cases are 0.0195, 0.0191, 0.0215, and 0.0222, respectively.

Table 5 RMSE for high forest

Incidence angles $\theta$	Case1	Case2	Case3	Case4
0°-10°	0.0288	0.0381	0.0258	0.0380
11°-20°	0.0280	0.0323	0.0273	0.0322
21°-30°	0.0278	0.0212	0.0260	0.0253
31°-40°	0.0236	0.0193	0.0244	0.0198
41°-50°	0.0197	0.0218	0.0251	0.0245
>50°	0.0315	0.0316	0.0315	0.0317
Final accuracy	0.0195	0.0191	0.0215	0.0222

## 5. Discussion

The algorithm presented in this paper heavily relies on the observation geometry, specifically the specular incidence angle. The inclusion of this information has significantly improved the final retrieval accuracy across all land surface types, including bare soil, low vegetation, and forest coverage areas. Table 5 provides a summary of the number of specular incidence angles observed, with most data distributed between  $20^\circ$  to  $40^\circ$ . The percentage of incidence angles at  $21^\circ$  and  $40^\circ$  is 24.66%, while the percentage between  $31^\circ$  and  $40^\circ$  is 26.87%. For incidence angles between  $11^\circ$  and  $20^\circ$ , the percentage is 17.97%, which is almost identical to the percentage for incidence angles between  $41^\circ$  and  $50^\circ$  (19.67%). However, there is less data available for small incidence angles or larger angles, with only 8.43% of observations falling within the  $0^\circ$ - $10^\circ$  range and 2.40% for incidence angles greater than  $50^\circ$ .

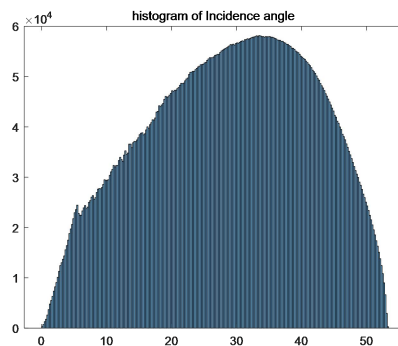


Figure 18. Histogram of incidence angles

Table 6. Percentages of incidence angles

Specular incidence angles	Percentage
0°-10°	8.43%
11°-20°	17.97%
21°-30°	24.66%
31°-40°	26.87%
41°-50°	19.67%
>50°	2.40%

## 6. Conclusion

In this paper, a soil moisture retrieval algorithm for FY-3E GNOS-R is presented. In particular, this method is based on the first order model which is commonly used for radiometer and here it was converted to the form of GNOS-R with the consideration of the correction of surface roughness, two way propagation attenuation and vegetation density. The vegetation effects on the surface reflectivity are all considered, while we evaluate the vegetation water content, opacity. Meanwhile, we evaluate the surface roughness on the final surface reflectivity. Soil moisture model is achieved through the evaluation of vegetation volume scattering by reformulating the first order model and also the effects of surface roughness are also amended by new coefficients. The global land cover types are divided by barren condition, low vegetation and high forest. Therefore, three kinds of retrieval algorithms are presented. By comparing the FY-3E GNOS-R soil moisture with the reference SMAP soil moisture data, good consistency is achieved: Unlike the normalized angle information inversion, the most significant improvement of the inversion algorithm in this paper is that the final inversion accuracy is improved by using the angle information. It is concluded that under different angles, the accuracy of soil moisture retrieval by roughness is effectively corrected according to the unique roughness of GNSS-R. The optimal inverse RMSE for barren condition is 0.0235 g/cm<sup>3</sup>. As for both low vegetation and high forest, we corrected the effects of vegetation density and two-way propagation path by achieving corresponding correctness coefficients. Good consistency is obtained with RMSE equals 0.0264 and 0.0191 for low vegetation and high forest, respectively. This work here focuses on

evaluating FY 3E GNOS-R as a complementary tool for global soil moisture estimation. Since the data is still under test, only one month data is employed. However, the results have fully proved that this kind of new GNSS-R data has the ability to achieve good soil moisture retrieval results. More importantly, this method presents the correction parameters of full roughness coefficients, vegetation density and two-way propagation path and they are fully oriented to GNOS-R.

## **ACKNOWLEDGEMENTS**

**Funding:**This research waas funded by the National Natural Science Foundation of China(No.42061057)

## References

1. Hall, C.D.; Cordey, R.A. Multistatic Scatterometry. In Proceedings of the International Geoscience and Remote Sensing Symposium, ‘Remote Sensing: Moving Toward the 21st Century’, Edinburgh, UK, 12 – 16 September 1988.<https://doi.org/10.1109/IGARSS.1988.570200>
2. Martin-Neira, M.A. Passive Reflectometry and Interferometry System (PARIS): Application to ocean altimetry. *ESA J.* 1993, 17, 331 – 355
3. Zavorotny, V.U.; Gleason, S.; Cardellach, E.; Camps, A. Tutorial on Remote Sensing Using GNSS Bistatic Radar of Opportunity. *IEEE Geosci. Remote Sens. Mag.* 2014, 2, 8 – 45,<https://doi.org/10.1109/MGRS.2014.2374220>.
4. Yan, Q., et al., Pan-tropical soil moisture mapping based on a three-layer model from CYGNSS GNSS-R data. *Remote Sensing of Environment*, 2020. 247: p. 111944.<https://doi.org/10.1016/j.rse.2020.111944>.
5. Carrenolueno, H., G. Luzi and M. Crosetto, Above-Ground Biomass Retrieval over Tropical Forests: A Novel GNSS-R Approach with CyGNSS. *Remote Sensing*, 2020. 12(9): p. 1368.<https://doi.org/10.3390/rs12091368>
6. Clara, C., J.T. Reager and S. Eric, CYGNSS data map flood inundation during the 2017 Atlantic hurricane season. *Scientific Reports*, 2018. 8(1): p. 9336-.<https://api.semanticscholar.org/CorpusID:49316442>
7. Carreno-Luengo, H. and C.R. Ruf, Mapping Freezing and Thawing Surface State Periods with the CYGNSS Based F/T Seasonal Threshold Algorithm. 2022.<https://doi.org/10.1109/JSTARS.2022.321646>
8. Gleason, S.; Adjrad, M.; Unwin, M. Sensing ocean, ice and land reflected signals from space: Results from the UK-DMC GPS reflectometry experiment. In Proceedings of the 18th International Technical Meeting of the Satellite Division of The Institute of Navigation, Palm Springs, CA, USA, 1 January 2005; pp. 1679 – 1685.TDS-1.
9. Mashburn J, Axelrad P, Lowe S T, et al. Global Ocean Altimetry with GNSS Reflections from TechDemoSat-1[J]. *IEEE Transactions on Geoscience and Remote Sensing*, 2018, 56(7): 4088–4097.<https://doi.org/10.1109/TGRS.2018.2823316>.
10. Ruf, C.S.; Chew, C.; Lang, T.; Morris, M.G.; Nave, K.; Ridley, A.; Balasubramaniam, R. A New Paradigm in Earth Environmental Monitoring with the CYGNSS Small Satellite Constellation. *Sci. Rep.* 2018, 8, 8782. <https://doi.org/10.1038/s41598-018-27127-4>.
11. W. Wan et al., "Initial Evaluation of the First Chinese GNSS-R Mission BuFeng-1 A/B for Soil Moisture Estimation," in IEEE Geoscience and Remote Sensing Letters, vol. 19, pp. 1-5, 2022, Art no. 8017305, doi: 10.1109/LGRS.2021.3097003.<https://doi.org/10.1109/LGRS.2021.3097003>
12. Unwin, M.J.; Pierdicca, N.; Cardellach, E.; Rautiainen, K.; Foti, G.; Blunt, P.; Guerriero, L.; Santi, E.; Tossaint, M. An Introduction to the HydroGNSS GNSS Reflectometry Remote Sensing Mission. *IEEE J. Sel. Top. Appl. Earth Obs. Remote Sens.* 2021, 99, 1.<https://doi.org/10.1109/JSTARS.2021.3089550>.
13. Sun, Y.; Huang, F.; Xia, J.; Yin, C.; Bai, W.; Du, Q.; Wang, X.; Cai, Y.; Li, W.; Yang, G.; et al. GNOS-II on Fengyun-3 Satellite Series: Exploration of Multi-GNSS Reflection Signals for Operational Applications. *Remote Sens.* 2023, 15, 5756. <https://doi.org/10.3390/rs15245756>
14. Shi, J., Dong, X., Zhao, T., Du, J., Jiang, L., Du, Y., Liu, H., Wang,Z., Ji, D., Xiong, C., “WCOM: the Science Scenario and Objectives of a Global Water Cycle Observation Mission,” *IEEE Geoscience and Remote Sensing Symposium*, pp.3646-3649,2014.<https://doi.org/10.1109/IGARSS.2014.6947273>.
15. Zhao, T., Shi, J., Lv, L., Xu, H., Chen, D., Cui, Q., Jackson, T.J., Yan, G., Jia, L., Chen, L., Zhao, K., Zheng, X., Zhao, L., Zheng, C., Ji, D., Xiong, C., Wang, T., Li, R., Pan, J., Wen, J., Yu, C., Zheng, Y., Jiang, L., Chai, L., Lu, H., Yao, P., Ma, J., Lv, H., Wu, J., Zhao, W., Yang, N., Guo, P., Li, Y., Hu, L., Geng, D., & Zhang, Z., “Soil moisture experiment in the Luan River supporting new satellite mission opportunities,” *Remote Sensing of Environment*, 2020.<https://doi.org/10.1016/j.rse.2020.111680>.
16. Entekhabi, D.; Njoku, E.G.; O’ Neill, P.; Kellogg, K.H.; Crow, W.; Edelstein, W.N.; Entin, J.K.; Goodman, S.D.; Jackson, T.J.; Johnson, J.; et al. The Soil Moisture Active Passive (SMAP) Mission. *Proc. IEEE* 2010, 98, 704 – 716.<https://doi.org/10.1109/JPROC.2010.2043918>.
17. Yan Q , Huang W , Jin S , et al. Pan-tropical soil moisture mapping based on a three-layer model from CYGNSS GNSS-R data. *Remote Sensing of Environment*, 2020, 247:111944.<https://doi.org/10.1016/j.rse.2020.111944>.
18. Chew C C , Small E E . Soil moisture sensing using spaceborne GNSS reflections: Comparison of CYGNSS reflectivity to SMAP soil moisture. *Geophysical Research Letters*, 2018, 45(9). <https://doi.org/10.1029/2018GL077905>.
19. Hyunglok K , Venkat L . Use of Cyclone Global Navigation Satellite System (CyGNSS) Observations for Estimation of Soil Moisture. *Geophysical Research Letters*, 2018, 45(16):8272-8282. <https://doi.org/10.1029/2018GL078923>
20. Clarizia M P , Pierdicca N , Costantini F , et al. Analysis of CYGNSS Data for Soil Moisture Retrieval[J]. *IEEE Journal of Selected Topics in Applied Earth Observations and Remote Sensing*, 2019, 12:2227 – 2235.<https://doi.org/10.1109/JSTARS.2019.2895510>
21. Yang, G.; Du, X.; Huang, L.; Wu, X.; Sun, L.; Qi, C.; Zhang, X.; Wang, J.; Song, S. An Illustration of FY-3E GNOS-R for Global Soil Moisture Monitoring. *Sensors* 2023, 23, 5825. <https://doi.org/10.3390/s23135825G>.

22. Entekhabi, D.; Njoku, E.G.; O' Neill, P.; Kellogg, K.H.; Crow, W.; Edelstein, W.N.; Entin, J.K.; Goodman, S.D.; Jackson, T.J.; Johnson, J.; et al. The Soil Moisture Active Passive (SMAP) Mission. Proc. IEEE 2010, 98, 704 – 716.<https://doi.org/10.1109/JPROC.2010.2043918>.
23. NASA EOSDIS Land Processes DAAC. Accessed 2022-10-06 from <https://doi.org/10.5067/MODIS/MCD12C1.006>.
24. Choudhury, T.J. Schmugge, A. Chang, R.W. Newton Effect of surface roughness on the microwave emission from soils. J. Geophys. Res., 89 (1979), pp. 5699-5706,<https://doi.org/10.1029/JC084iC09p05699>
25. R. Bindlish and A. P. Barros, “Parameterization of vegetation backscatter in radar-based, soil moisture estimation,” Remote Sens. Environ., vol. 76,no. 1, pp. 130 – 137, Apr. 2001.[https://doi.org/10.1016/S0034-4257\(00\)00200-5](https://doi.org/10.1016/S0034-4257(00)00200-5).



## Figure Legends

[Insert Figure Legends here]

要求：将文中所有图题和图例放在此页。按照在正文中引用的顺序排列。

Fig. 1 The development of space-borne GNSS-R missions or payloads.

Fig. 2 FY3E GNOS-R Non-Uniform DDM measurement.

Fig. 3 Specular reflection points of FY-3E GNOS-R on August 10, 2021. while the colorbar on the right hand indicate the SR of GNOS-R.

Fig. 4 global land cover and land use map

cover types

Fig. 6 Relationship between bare soil surface reflectivity and specular incidence angle. The lines with different colors represent different surface roughness conditions, as indicated in the legend. The surface root-mean-squared height is denoted by "s". The volumetric soil moisture content in subfigures (a), (b), and (c) are 0.1, 0.3, and 0.5, respectively. The clay fraction for both conditions is 50%.

Fig. 7 Illustration of zero-order model(a) and first-order model(b)

Fig. 8 Scattering features of zero-order model: transmissivity (a) and surface reflectivity versus the specular incidence angles(b,c); while the soil clay fraction and s for both figure b and c are 0.5 and 0.1, respectively. and the soil moisture content for figure b is 0.3, while the one for figure c is 0.5.

Fig. 9 Scattering features of first-order model. The vegetation volumes scattering reflectivity as shown in Equation 6 is shown in figure a. while the total surface reflectivity are presented in figure b and c and the clay fraction and s are 0.5 and 0.1 for, respectively. while the soil moisture content for figure b is 0.3, and the one for figure c is 0.5.

Fig. 10 Flowchart for FY-3E GNOS-R soil moisture retrieval

Fig. 11 Comparisons between SMAP roughness coefficients and the ones of GNOS-R for different incidence angles  $\theta$

Fig. 12 Values of vegetation density correction parameter A for four cases.

Fig. 13 Values of two-way propagation path correction parameter B for four cases

Fig. 14 Values of surface roughness correction parameter C for four cases.

Fig. 15. Forest density correction coefficient (A)

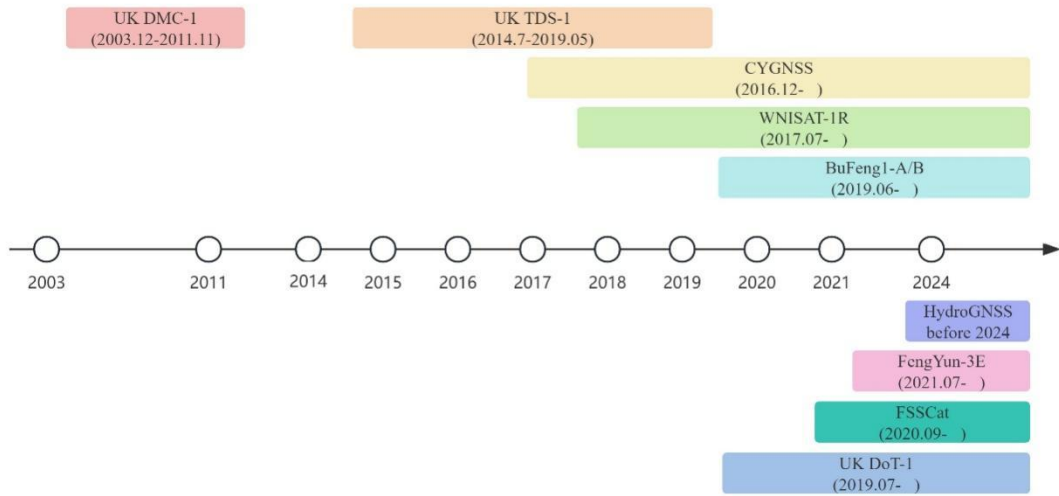
Fig. 16 Two-way propagation path correction parameter B

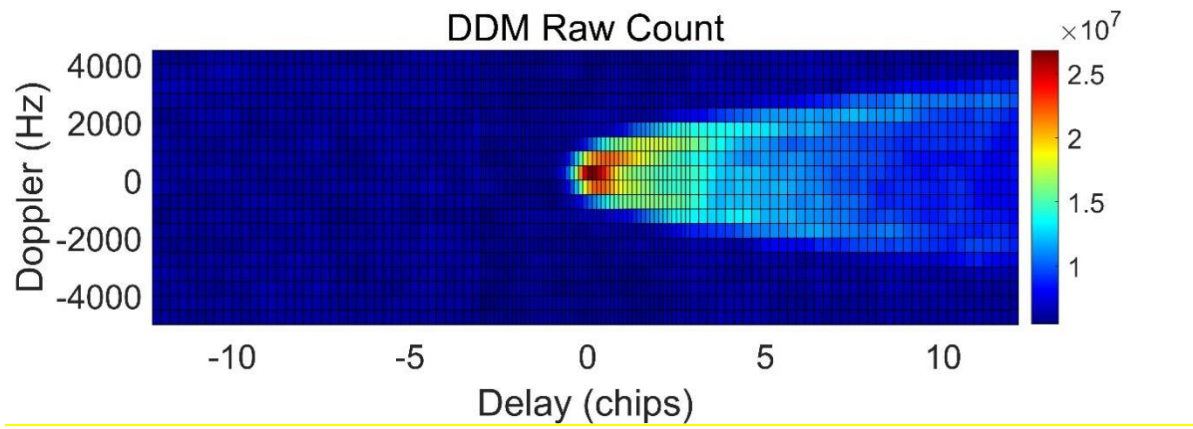
Fig. 17 roughness correction coefficients C for four cases

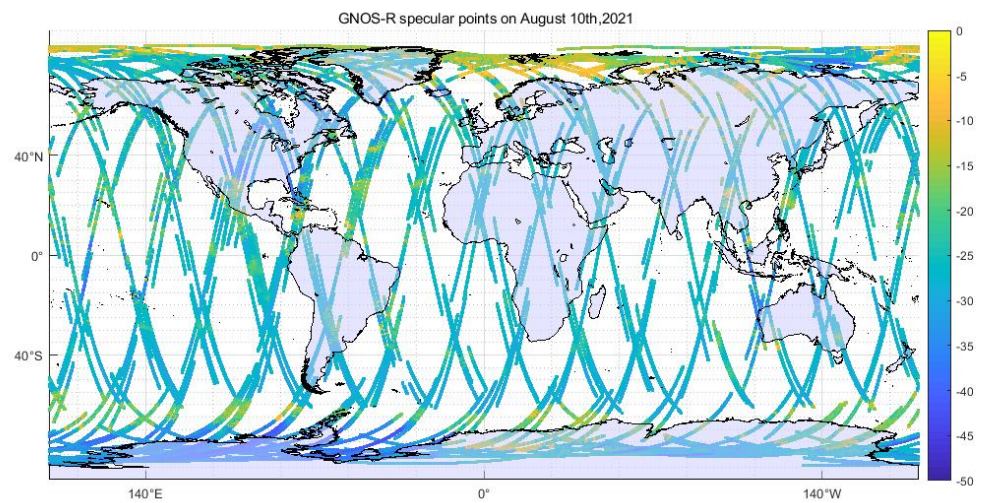
Fig. 18. Histogram of incidence angles

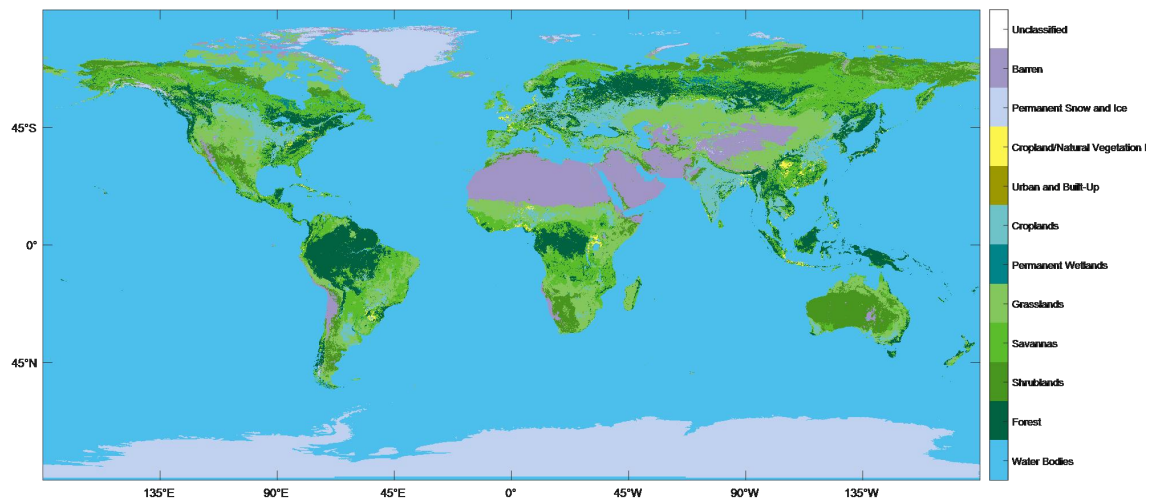
.....

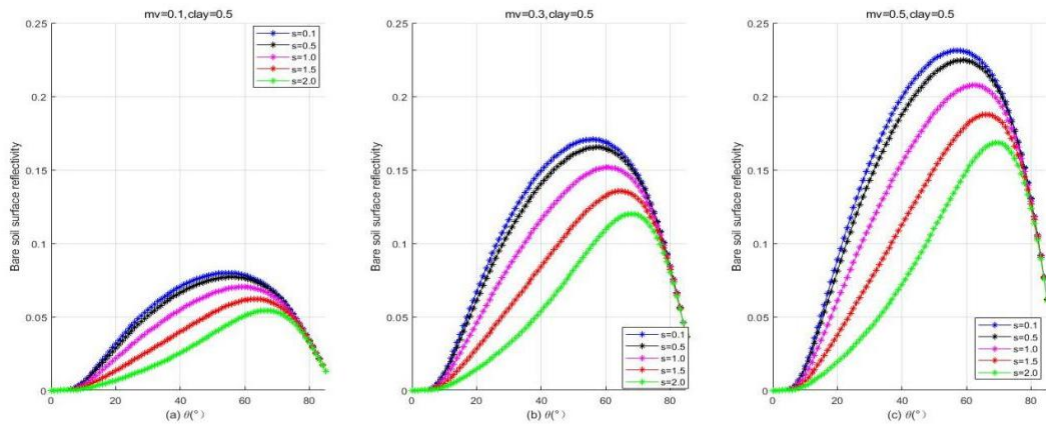
## Figures

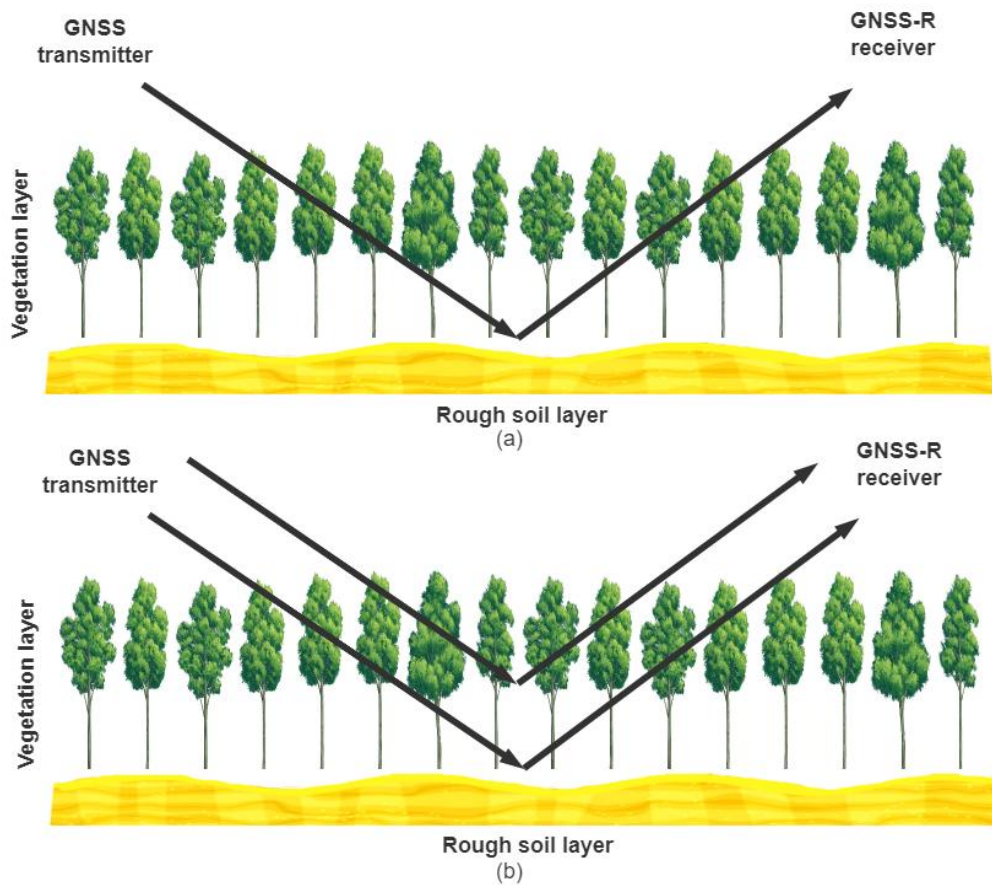


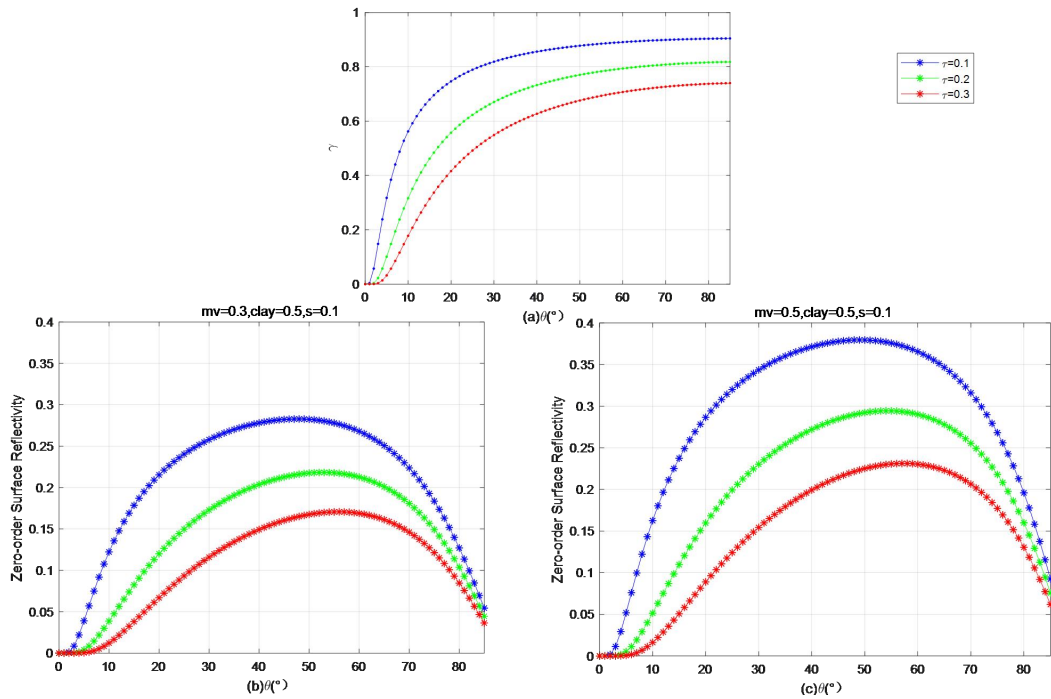


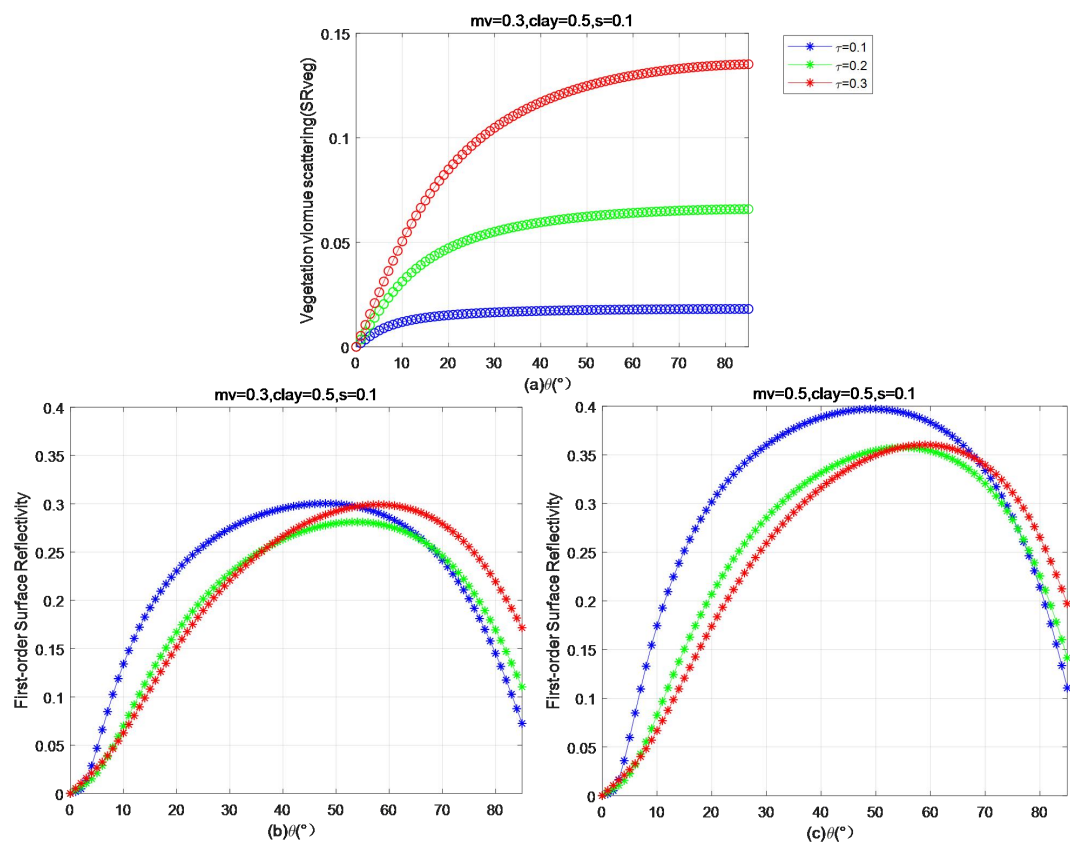


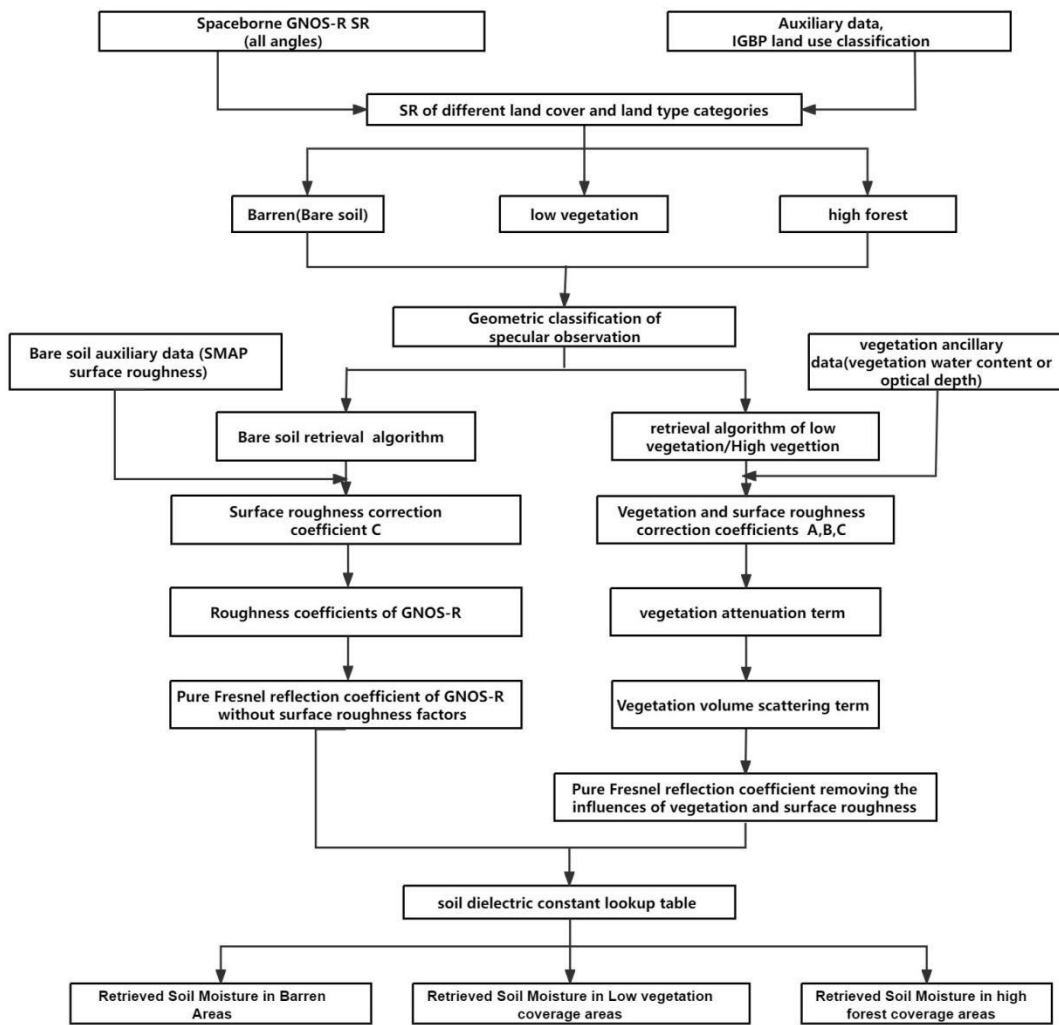


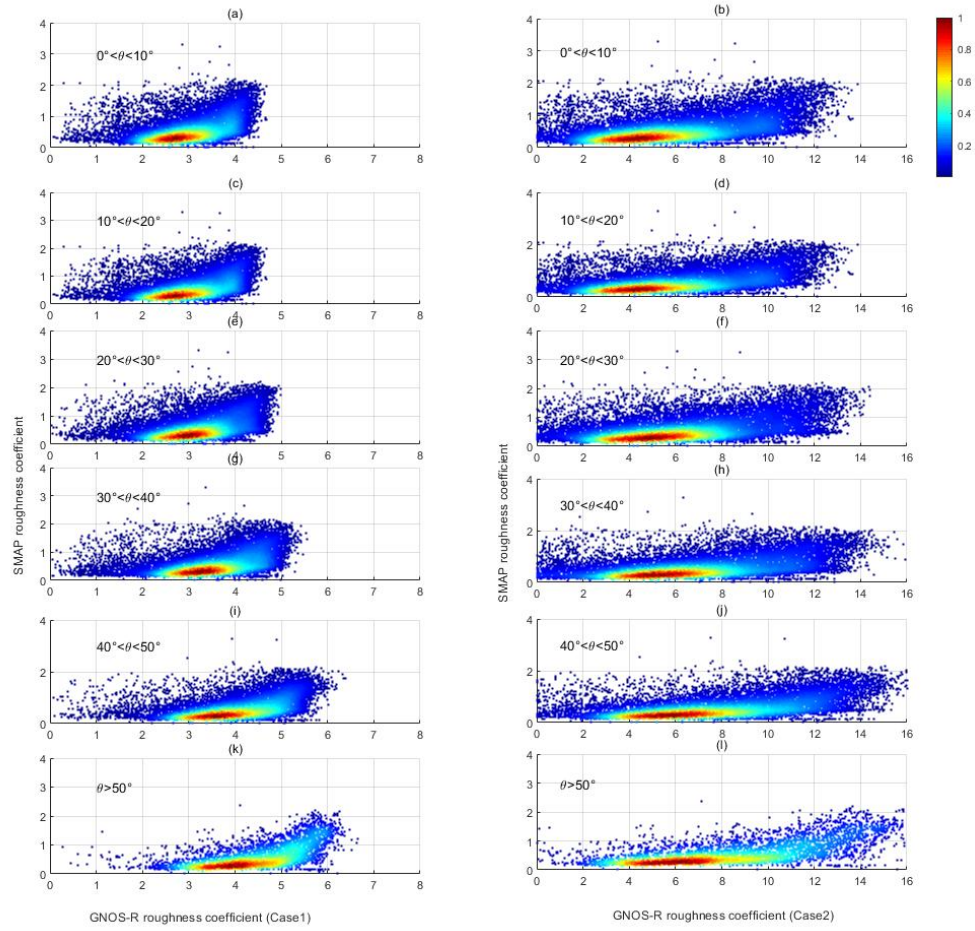


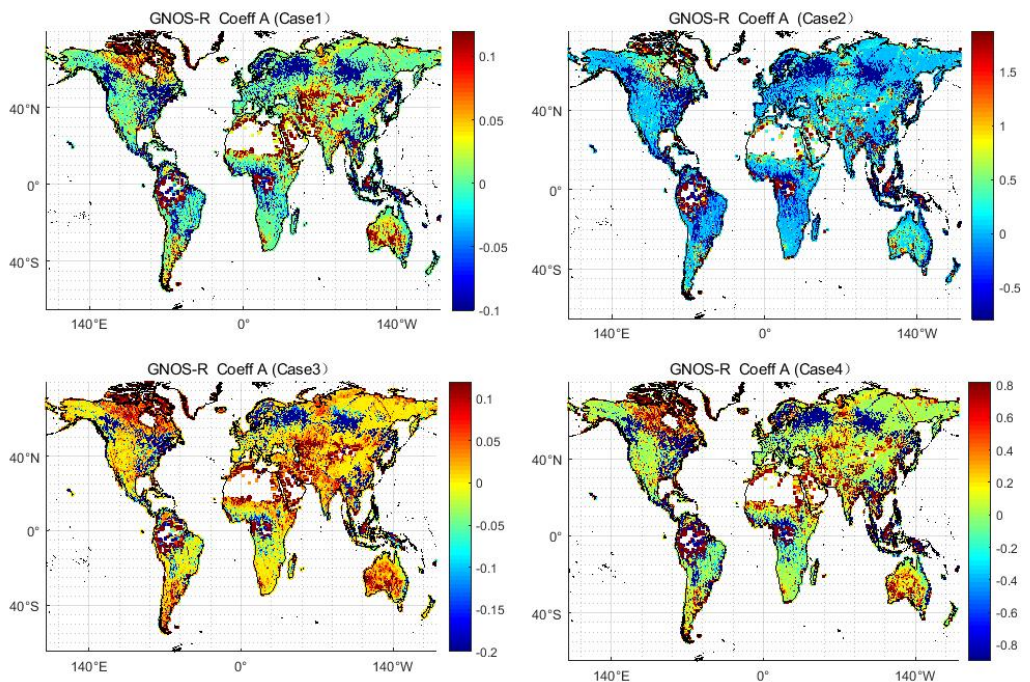


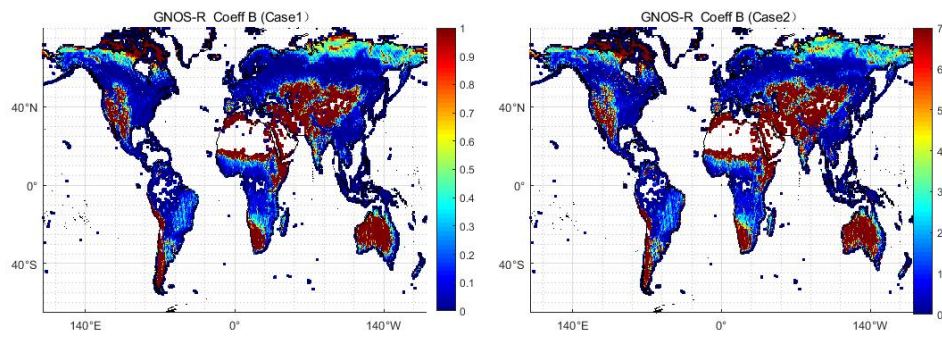


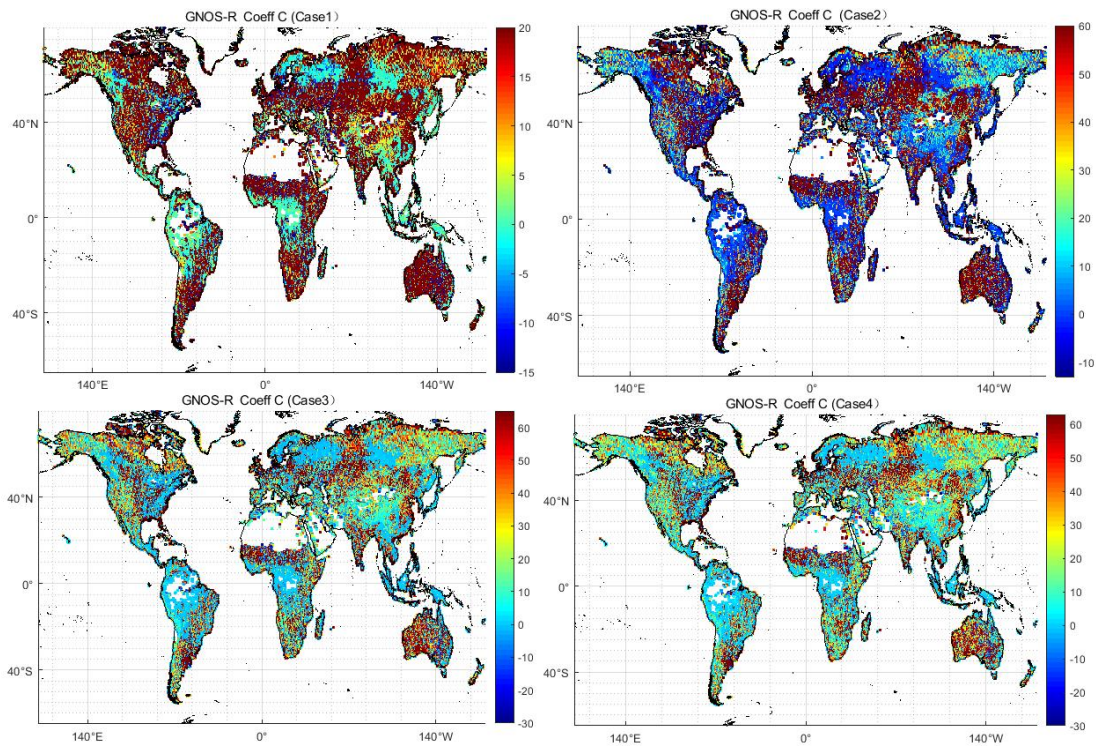


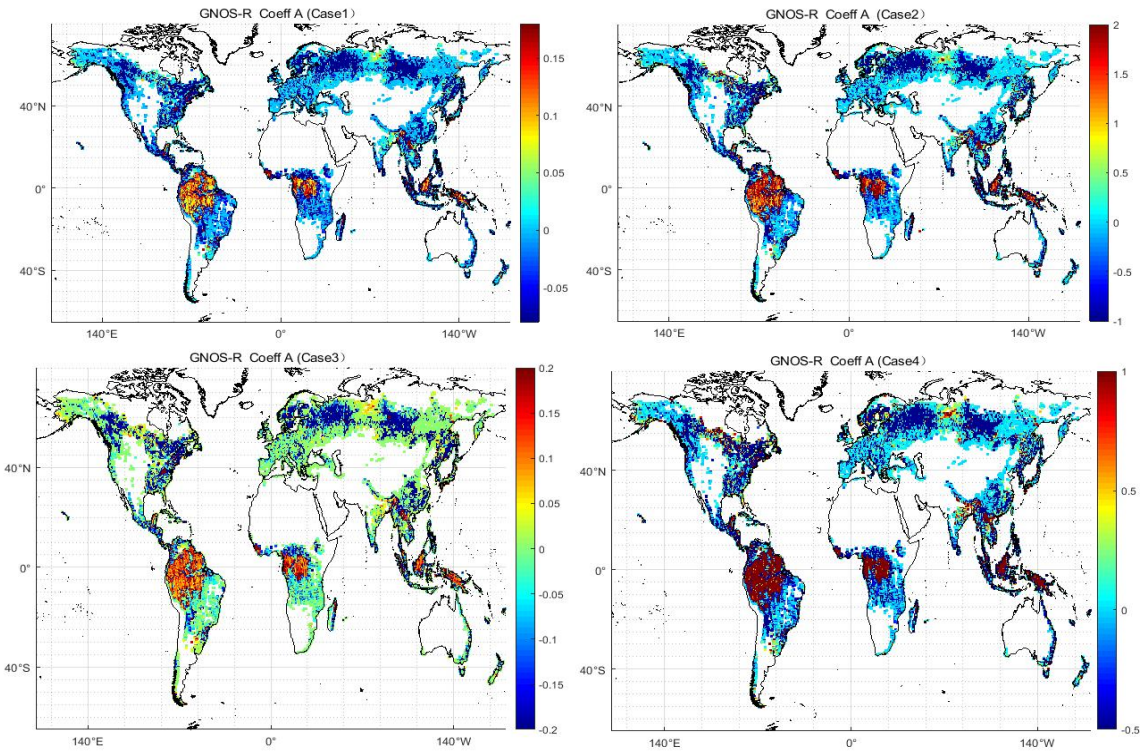


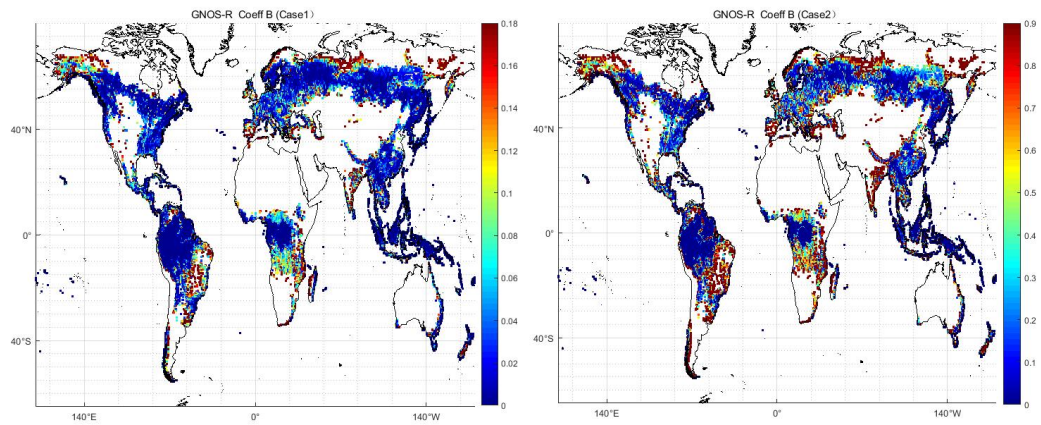


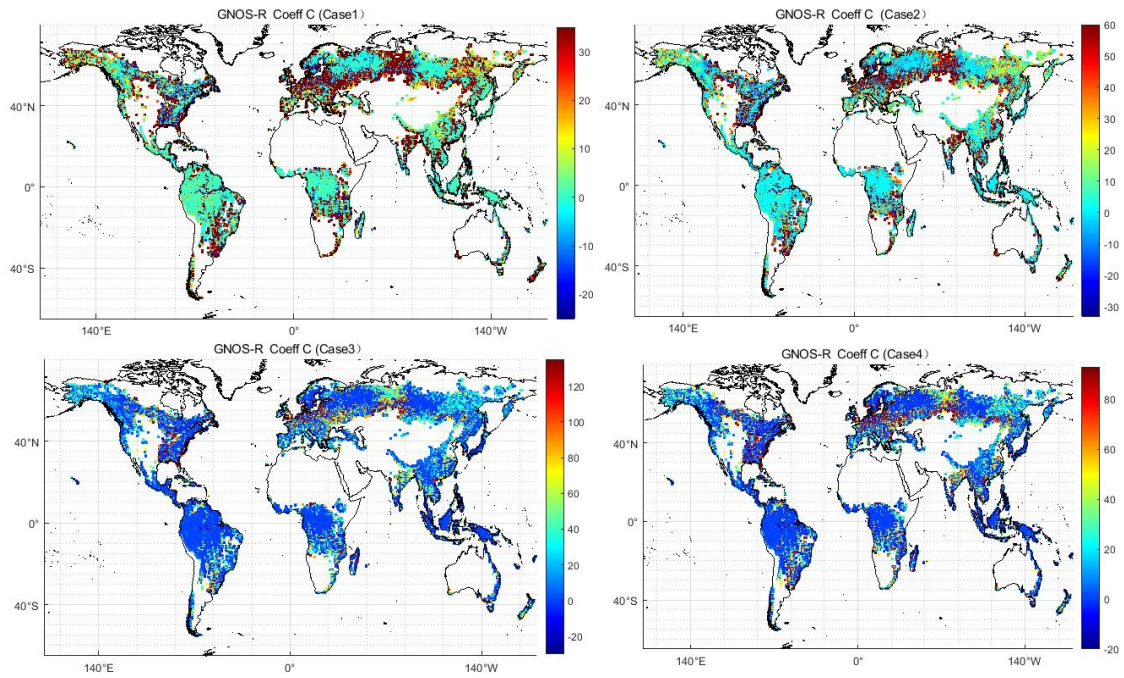


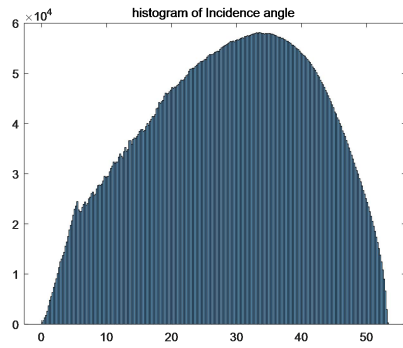












## Tables

Table 1 MCD12Q1 International Geosphere-Biosphere Program (IGBP) legend and re-classified land

Name	Value	New classifications
Evergreen Needleleaf Forests	1	Forest
Evergreen Broadleaf Forests	2	Forest
Deciduous Needleleaf Forests	3	Forest
Deciduous Broadleaf Forests	4	Forest
Mixed Forests	5	Forest
Closed Shrublands	6	Forest
Open Shrublands	7	Low-Vegetation
Woody Savannas	8	Low-Vegetation
Savannas	9	Low-Vegetation
Grasslands	10	Low-Vegetation
Permanent Wetlands	11	Low-Vegetation
Croplands	12	Low-Vegetation
Urban and Built-up Lands	13	Abandoned-type
Cropland/Natural Vegetation Mosaics	14	Low-Vegetation
Permanent Snow and Ice	15	Abandoned-type
Barren	16	Barren
Water Bodies	17	Abandoned-type
Unclassified	255	Abandoned-type

Table 2. GNOS-R surface roughness coefficients for different observation geometry of two cases.

Observation geometry $\theta$	Case 1	Case 2
0°-10°	1.4-4	1.5-11
11°-20°	2.1-4.5	2.1-12
21°-30°	2.2-4.8	2.2-13
31°-40°	2.2-5.5	2.2-14
41°-50°	2.5-5.5	2.5-14.5
>50°	3-5.5	4-14.1

Table 3. Soil moisture retrieval accuracy of RSME

Incidence angles $\theta$	RMSE(Case1)	RMSE(Case 2)
0°-10°	0.0061	0.0057
11°-20°	0.0259	0.0252
21°-30°	0.0245	0.0205
31°-40°	0.0214	0.0161
41°-50°	0.0180	0.0111
>50°	0.0055	0.0048
Combination Considerations of incidence angles separation	0.0235	0.0224

Table 4 RMSE for low vegetation coverage areas

Incidence angles $\theta$	Case1	Case2	Case3	Case4
0°-10°	0.0361	0.0447	0.0336	0.0440
11°-20°	0.0358	0.0390	0.0390	0.0410
21°-30°	0.0359	0.0330	0.0332	0.0331
31°-40°	0.0332	0.0300	0.0307	0.0283
41°-50°	0.0300	0.0261	0.0379	0.0340
>50°	0.0470	0.0301	0.0306	0.0310
Combination Considerations of incidence angles separation	0.0296	0.0290	0.0305	0.0316

Table 5 RMSE for high forest

Incidence angles $\theta$	Case1	Case2	Case3	Case4
0°-10°	0.0288	0.0381	0.0258	0.0380
11°-20°	0.0280	0.0323	0.0273	0.0322
21°-30°	0.0278	0.0212	0.0260	0.0253
31°-40°	0.0236	0.0193	0.0244	0.0198
41°-50°	0.0197	0.0218	0.0251	0.0245
>50°	0.0315	0.0316	0.0315	0.0317
Final accuracy	0.0195	0.0191	0.0215	0.0222

Table 6. Percentages of incidence angles

Specular incidence angles	Percentage
0°-10°	8.43%
11°-20°	17.97%
21°-30°	24.66%
31°-40°	26.87%
41°-50°	19.67%
>50°	2.40%